A&A, 715, A358 (2026)
https://doi.org/10.1051/0004-6361/202662676
© The Authors 2026

Astronomy & Astrophysics

Gaia Science Alerts microlensing events with mass estimates verifiable in *Gaia* Data Release 4

M. Wicker[1,2,⋆], Ł. Wyrzykowski[1,3], M. Hundertmark[4], K. Kruszyńska[5], E. Bachelet[6], P. Zieliński[7], M. Kalicki[7], K. Kotysz[1,8], P. J. Mikołajczyk[3,8], M. Gromadzki[1], K. Howil[1], J. Majumdar[1], N. Ihanec[2], M. Jabłońska[1,9], M. Ratajczak[1], M. Sitek[1], E. Stonkutė[10], M. Maskoliūnas[10], E. Pakštienė[10], J. Zdanavičius[10], V. Čepas[10], U. Jonauskaitė[10], V. Bozza[11,12], A. Cassan[13], M. Dominik[14], R. Figuera Jaimes[15,16], M. Rabus[17], P. Rota[11,12], K. A. Rybicki[1], R. A. Street[5], Y. Tsapras[4], J. Wambsganss[4] (The OMEGA Key Project), S. Awiphan[18], T. Butterley[19], U. Burgaz[20], J. M. Carrasco[21,22,23], F. Cusano[24], V. S. Dhillon[25,26], R. Wilson[19], H. H. Esenoğlu[27], A. Garofalo[24], M. Jelínek[28], F. Lewis[29,30], U. Pylypenko[31,32], J.-P. Rivet[33], O. Tasuya[18], P. Trzcionkowski[1] (BHTOM Team), F. Abe[34], D. P. Bennett[35,36], A. Bhattacharya[35,36], I. A. Bond[37], K. Daimon[38], R. Hamada[38], Y. Hirao[39], S. Makida[38], S. Ishitani Silva[40,35], S. Miyazaki[41], Y. Muraki[34], T. Nagai[38], K. Nunota[38], R. Ogawa[38], R. Oishi[38], H. Ose[38], G. Olmschenk[35], C. Ranc[13], N. J. Rattenbury[42], Y. K. Satoh[43], T. Sumi[38], D. Suzuki[38], T. Tamaoki[38], S. K. Terry[35,36], C. Ueda[38], P. J. Tristram[44], A. Vandorou[35,36], and H. Yama[38] (MOA collaboration)

(Affiliations can be found after the references)

Received 21 August 2026 / Accepted 16 October 2026

ABSTRACT

Gaia Science Alerts provide an all-sky stream of photometric transients, including events consistent with gravitational microlensing. For such events, forthcoming epoch astrometry from the *Gaia* mission offers the possibility of testing photometric lens mass predictions. While microlensing parallax inferred from the photometric light curve can constrain the event geometry, a direct lens mass measurement additionally requires the angular Einstein radius, which may be accessible through astrometric microlensing. We aim to construct a pre-Data-Release-4 (DR4) sample of *Gaia* microlensing events for which the available photometry provides a measurable microlensing-parallax signal. This allows us to derive statistical predictions for the lens mass and distance. We forward-modelled these events to predict the detectability of the astrometric microlensing signal in *Gaia* DR4. We identify 56 *Gaia* Science Alerts microlensing events with 71 point-source point-lens solutions with annual parallaxes that satisfy our fit-quality, posterior-boundedness, and parallax-significance criteria. Lens masses and distances were inferred using two prior-based frameworks, pyLIMASS and the Besançon Galaxy Model, which combine the measured microlensing parameters and *Gaia* source information with stellar-population and Galactic models. These inferred parameters were used to simulate *Gaia* DR4-like along-scan astrometry and estimate the detectability of the astrometric microlensing signal. The inferred lens masses and distances remain strongly prior-dependent without a direct angular Einstein radius measurement. Among the 284 event–solution–prior branches, 47 are classified as high-confidence astrometric detections using *Gaia* DR4-like simulations. These predictions can be tested once epoch astrometry is released in *Gaia* DR4.

Key words. gravitational lensing: micro – astrometry – stars: fundamental parameters

1. Introduction

Gravitational microlensing occurs when a foreground lens passes sufficiently close to the line of sight of a background source, producing transient magnification (Paczyński 1986; Gould 2000). Because the signal is gravitational rather than radiative, microlensing is sensitive to lenses regardless of their luminosity and, therefore, provides a unique probe of faint or non-luminous objects. This includes low-mass stars, isolated stellar remnants (Sahu et al. 2022), planets, and free-floating planetary-mass objects.

Since the first detections in the early 1990s, microlensing has been driven primarily by photometric monitoring: first by surveys such as MACHO, EROS, and OGLE (Alcock et al. 1993; Aubourg et al. 1993; Udalski et al. 1993), and later by dedicated high-cadence Galactic-bulge surveys such as OGLE, MOA, KMTNet, and PRIME (Udalski et al. 2015; Bond et al. 2001; Kim et al. 2016; Sumi et al. 2025). This is complemented by wide-field transient surveys such as ASAS-SN, ATLAS, *Gaia*, VVV, and ZTF (Shappee et al. 2014; Tonry et al. 2018; Gaia Collaboration 2016; Minniti et al. 2010; Bellm et al. 2019). In the coming decade, the Vera C. Rubin Observatory's Legacy Survey of Space and Time (LSST) and the Nancy Grace Roman Space Telescope will further transform the field. The Rubin observatory will provide wide-field optical monitoring across much of the southern sky, while the Roman telescope will conduct high-precision near-infrared time-domain observations through the Roman Galactic Bulge Time Domain Survey and the Roman Galactic Plane Survey, delivering large new samples of microlensing events (Ivezić et al. 2019; Penny et al. 2019).

⋆ Corresponding author: mwicker@astrouw.edu.pl

Open Access article, published by EDP Sciences, under the terms of the Creative Commons Attribution License (https://creativecommons.org/licenses/by/4.0), which permits unrestricted use, distribution, and reproduction in any medium, provided the original work is properly cited.
This article is published in open access under the Subscribe to Open model. Subscribe to A&A to support open access publication.

The physical scale and duration of a microlensing event are determined by three fundamental quantities: the lens mass (M_L), the lens–source relative parallax (π_{rel}), and the lens–source relative proper-motion vector ($\boldsymbol{\mu}_{rel}$). These determine the angular Einstein radius ($\theta_E = (\kappa M_L \pi_{rel})^{1/2}$), and the Einstein timescale ($t_E = \theta_E/\mu_{rel}$), where $\mu_{rel} = |\boldsymbol{\mu}_{rel}|$ and $\kappa = 4G/(c^2\,\mathrm{au})$. The microlensing-parallax vector ($\boldsymbol{\pi}_E$) has magnitude $\pi_E = \pi_{rel}/\theta_E$ and points in the direction of $\boldsymbol{\mu}_{rel}$. Photometric light curves generally constrain t_E and, when higher-order distortions are detected, $\boldsymbol{\pi}_E$, but these quantities alone do not provide a direct measurement of the lens mass or distance.

Additional constraints can be obtained from annual or satellite microlensing parallaxes, finite-source effects, lens-flux constraints, spectroscopic characterisation of the source star, high-resolution imaging, interferometric observations, and astrometric microlensing. In particular, combining the microlensing-parallax amplitude with the angular Einstein radius yields the lens mass directly through $M_L = \theta_E/(\kappa\pi_E)$ (Gould 2000). Astrometric microlensing produces a displacement of the centroid of light of the combined unresolved lensed images relative to the unlensed source position. Because the amplitude of this displacement is proportional to θ_E, modelling the astrometric trajectory provides a measurement of the angular Einstein radius (Dominik & Sahu 2000). Combining photometric and astrometric microlensing measurements can therefore constrain the lens mass and distance and break degeneracies inherent in photometric-only models.

Gaia is uniquely suited to studying microlensing events. The mission combines homogeneous all-sky photometry with high-precision astrometry and spectroscopic information for over two billion sources (Gaia Collaboration 2016). The *Gaia* Science Alerts (GSA) system has identified and published ongoing photometric transients in near real time, enabling ground-based follow-up while transients continue to evolve (Hodgkin et al. 2021). For microlensing, *Gaia* is particularly complementary to ground-based bulge surveys because it covers the Galactic disc and higher-latitude fields, where events can be bright, appear relatively nearby, and favour astrometric lensing (Belokurov & Evans 2002). *Gaia* Data Release 3 (DR3) has already delivered the first all-sky catalogue of *Gaia* microlensing candidates (Wyrzykowski et al. 2023) with multiple dark lens candidates (Kruszyńska et al. 2024).

Gaia photometry has contributed to a diverse set of microlensing discoveries, including planetary events such as Gaia22dkvLb (Wu et al. 2024), AT2021ueyLb/Gaia21dnc (Ban et al. 2025), and Gaia23bra b (Harris et al. 2026), long-timescale dark-lens candidates such as Gaia18cbf (Kruszyńska et al. 2022) and Gaia18ajz (Howil et al. 2025), high-magnification events with a complementary space-parallax signal such as Gaia19bld (Rybicki et al. 2022), and binary-lens events with full Keplerian orbital solutions such as Gaia16aye (Wyrzykowski et al. 2020) and Gaia20fnr (Wicker et al. 2026). *Gaia* data have also contributed to the identification of very short-timescale events associated with free-floating or wide-orbit planetary-mass lenses, such as KMT-2024-BLG-0792/OGLE-2024-BLG-0516 (Dong et al. 2026). For *Gaia* DR3-ULENS-001, the anomalous *Gaia* DR3 astrometric parameters are consistent with the astrometric microlensing signal predicted by simulations based on the photometric model. This agreement suggests a nearby isolated white dwarf as the lens (Jabłońska et al. 2022). Many more such events are expected in *Gaia* Data Release 4 (DR4)[1], where epoch astrometric and photometric data will be available for all sources. The long *Gaia* astrometric time series, paired with photometric data from other surveys or follow-up observations, makes *Gaia* sensitive to long-timescale microlensing events, such as those from isolated black holes (Rybicki et al. 2018).

In this study, we constructed a pre-DR4 benchmark sample of microlensing events discovered through GSA. We considered alerts issued before the *Gaia* DR4 time cut, identified events consistent with microlensing after automated filtering, cross-matching, modelling, and visual vetting, and focused on the subset for which the available photometry supports a point-source point-lens (PSPL) model with annual parallax. We fitted the photometric models to the combined *Gaia* and follow-up data and separately to the *Gaia*-only light curves to quantify the role of complementary monitoring. We then inferred lens mass and distance posteriors using both a Galactic-prior and a Gaussian-mixture approach. Using these inferred lens properties, we forward-modelled the astrometric microlensing signals expected in *Gaia* DR4. Our goal is to provide testable pre-DR4 mass predictions and identify the *Gaia*-alert events for which future *Gaia* astrometry is most likely to verify the microlensing scenario.

This paper is organised as follows. In Sect. 2, we describe the GSA parent sample, follow-up data, and event-selection procedure. In Sect. 3, we present the photometric model and the treatment of parallax solutions. In Sect. 4, we summarise the sample of the final photometric models, which we compare to *Gaia*-only models in Sect. 5. In Sect. 6, we present the lens mass and distance estimates, and in Sect. 7 we predict the expected *Gaia* DR4 astrometric microlensing signals. We discuss the implications and limitations of the sample and summarise our conclusions in Sect. 8.

2. Parent sample, data, and event selection

2.1. Parent sample from Gaia Science Alerts

The starting point for our catalogue of gravitational microlensing events for which epoch astrometric data will be released in *Gaia* DR4 was the full public archive of GSA. This archive provides a real-time transient stream generated from *Gaia* photometric observations (Hodgkin et al. 2021). The archive contains 27 076 alerts covering the entire *Gaia* mission lifetime. Each alert entry provides a uniform set of metadata, including the alert identifier, alert date, equatorial coordinates, alert magnitude, historical source brightness and scatter, assigned transient class, publication flag, comments, and transient name server (TNS) identifier when available. In addition, the alert pages provide the *Gaia* *G*-band light curves. Although per-epoch BP/RP spectra are displayed on the GSA webpages, these are not distributed in a calibrated form suitable for homogeneous use in the present analysis and were therefore not used further. All *Gaia* photometric models in this work are based on the calibrated *Gaia* *G*-band measurements released through the alert system.

The archive metadata are informative but were not adopted as hard selection criteria. There are 45 unique class labels in GSA. Among the 27 076 alerts in the full archive, only 42 alerts carry the explicit `ULENS` class label. Likewise, the free-text comment field contains the string ‘ulens’ or related lensing annotations for 715 alerts in the full archive. Importantly, both the class labels and comments reflect the information available at or around the time the alert was issued, when the transient light curve was often still sparsely sampled and its nature uncertain. Microlensing events can therefore be difficult to recognise reliably at this early stage, particularly before the characteristic light-curve

[1] Expected 2 December 2026.

Table 1. Sequential selection of the GSA microlensing sample.

Step	Selection criterion	Sect.	Retained	Removed
1	Full GSA archive	2.1	27 076	–
2	Alert issued before the DR4 cut-off (2020 January 20, 22:00 UTC)	2.2	11 048	16 028
3	At least ten *Gaia G*-band measurements	2.3	4839	6209
4	Unblended *Gaia*-only PSPL fit converges	3.1	2665	2174
5	≥2 *Gaia* points within $t_0 \pm t_E$ and ≥5 outside	3.1	513	2152
6	Cross-matching, external photometry, visual vetting	3.2	229	284
7	Acceptance of PSPL models with parallax and remaining exclusions	3.3–4	56	173

morphology is fully developed. This illustrates the heterogeneous nature of real-time alert classification: potentially relevant microlensing events may carry the dedicated `ULENS` label, may only be mentioned in the comments, or may remain classified under another transient class. We therefore did not pre-select targets on the basis of the archive classification alone.

2.2. Temporal cut and relevance to DR4

According to the current public *Gaia* DR4 content summary[2], DR4 is based on observations acquired between 25 July 2014 at 10:30 UTC and 20 January 2020 at 22:00 UTC, corresponding to a 66-month data interval. As the present work is motivated by the prospect of complementing photometric microlensing models derived from GSA with astrometric information expected in *Gaia* DR4, the alert sample was restricted to events whose GSA alert was issued before the DR4 cut-off. This reduced the sample from 27 076 to 11 048 alerts.

Alerts issued after the DR4 cut-off were not considered, because their most informative microlensing epochs are unlikely to be represented in the DR4 astrometric time series. For long events, the main astrometric perturbation may occur after the final DR4 observation. For short events, the alert may occur too late for *Gaia* to have sampled the centroid shift sufficiently before the cut-off. By contrast, alerts issued before the cut-off offer the possibility that at least a substantial fraction of the relevant astrometric trajectory is represented within the DR4 time-series products. We emphasise that this choice introduces a time-dependent selection effect. The sample studied here is not intended to represent the full *Gaia* microlensing alert population. Rather, it represents the subset of alerts that pass the selection criteria described below and for which a pre-DR4 photometric model can, in principle, be tested against the forthcoming astrometric time-series data.

2.3. Gaia time-series data

For each focal-plane crossing, *Gaia* observes a source photometrically, astrometrically, and spectroscopically. The *Gaia* G-band alert light curves therefore provide the epochs at which *Gaia* astrometric information is also expected to be available in DR4. Even when a microlensing light curve can be well constrained by ground-based follow-up observations, the astrometric microlensing signal is measurable by *Gaia* only if it observed the source at a time near or during the magnified period. We therefore required a minimum number of *Gaia* G-band measurements in the alert light curve before considering an event for astrometric-signal predictions.

We retained only alerts with at least ten *Gaia* G-band measurements published through the GSA webpages. This cut also removes very faint events that were not detected by *Gaia* before the brightening that caused the alert. These events, Gaia17bzy and Gaia19dqr, therefore lack a *Gaia* DR3 source ID. The cut reduced the pre-DR4 alert sample from 11 048 to 4 839 candidate events for which we considered microlensing models. The sequential selection procedure of the full sample is listed in Table 1.

3. Photometric modelling and final sample construction

From our sample of GSA events, we identified candidate microlensing events by following a hierarchical procedure. We first used the *Gaia* alert photometry alone to identify light curves broadly compatible with a PSPL morphology. We then used catalogue cross-matches, external photometry, and visual inspection to remove clear contaminants and complex events. Finally, we performed homogeneous PSPL modelling with and without annual parallax on the vetted sample. This strategy follows the same general logic as previous large-scale *Gaia* microlensing searches (Kruszyńska et al. 2024). All microlensing models were fitted with `pyLIMA`[3] (Bachelet et al. 2017).

3.1. Initial Gaia-only PSPL screening

We adopted the standard PSPL model. For rectilinear lens–source motion, the instantaneous angular separation between the lens and source, in units of the angular Einstein radius, is

$$u(t) = \left[u_0^2 + \left(\frac{t - t_0}{t_E} \right)^2 \right]^{1/2}, \tag{1}$$

where t_0 is the time of closest approach, u_0 is the signed minimum lens–source separation in units of θ_E, and t_E is the Einstein-radius crossing time. The corresponding PSPL magnification is

$$A(u) = \frac{u^2 + 2}{u\sqrt{u^2 + 4}}. \tag{2}$$

For each independent telescope and filter dataset j, the model flux is

$$F_j(t) = f_{s,j} A[u(t)] + f_{b,j}, \tag{3}$$

where $f_{s,j}$ is the unmagnified source flux and $f_{b,j}$ is the unresolved blend flux. The flux coefficients were determined independently for each telescope and filter dataset.

For the initial screening, we used only the *Gaia G*-band light curves published through the GSA pages. We first fitted

[2] https://www.cosmos.esa.int/web/gaia/data-release-4

[3] https://github.com/ebachelet/pyLIMA

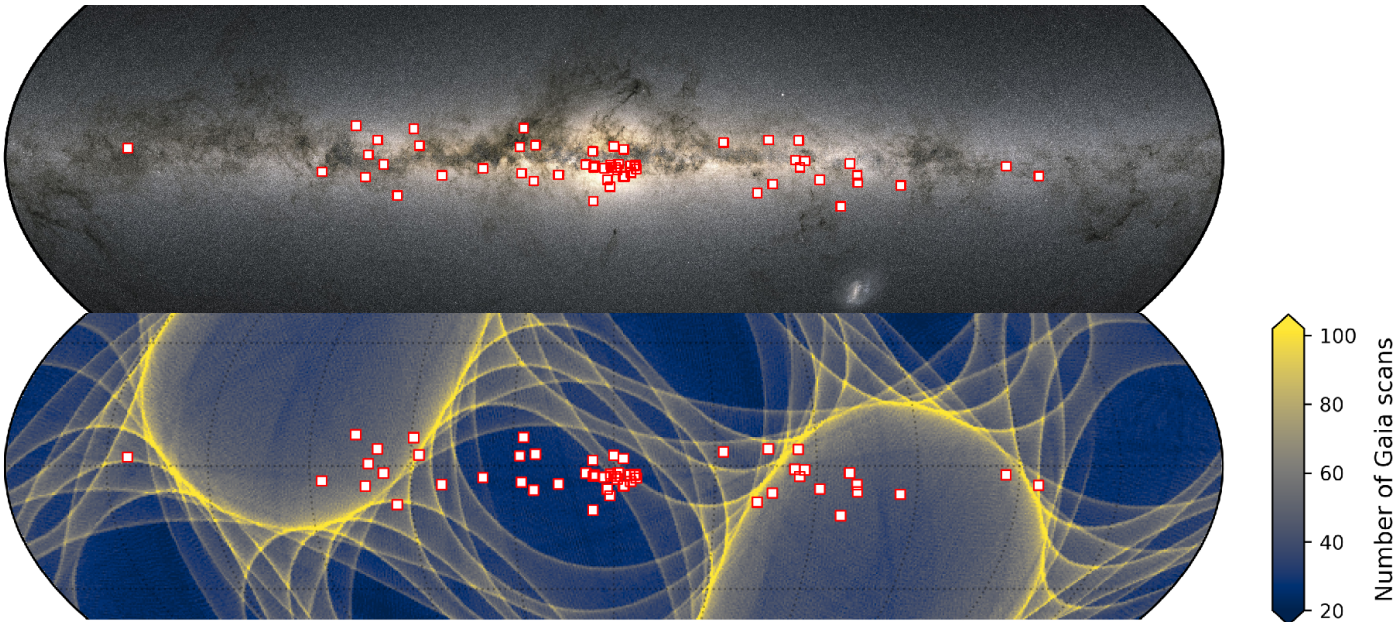

Fig. 1. Sky map view of the Milky Way (top) and *Gaia* DR3 nominal scanning law map (bottom). The locations of the final sample of microlensing events are marked with red squares. The figures were made using `MW-Plot`, *Gaia* EDR3 data (Gaia Collaboration 2021), and `gaiaunlimited`.

an unblended PSPL model with a Levenberg–Marquardt optimiser (Levenberg 1944; Marquardt 1963), using the parameters $(t_0, u_0, t_E, f_{s,Gaia})$. The resulting solution was used only to initialise subsequent trust region reflective fits. We ran both blended and unblended optimisations at this stage but adopted the unblended solution for the automated screening because the blend term is poorly constrained for many sparsely sampled *Gaia*-only light curves and can otherwise drive unstable preliminary solutions. Blending was included again in all final modelling steps.

A GSA alert was retained as a preliminary microlensing candidate if the unblended *Gaia*-only PSPL fit converged to a finite solution. This reduced the pre-selected GSA alert sample from 4839 to 2665. We then required the fitted light curve to contain at least two *Gaia* measurements within $t_0 \pm t_E$ and at least five measurements outside this interval. These baseline measurements may lie on either side of the event. We did not require *Gaia* baseline coverage both before and after the magnified part of the light curve. This avoids removing long-timescale events and events whose magnified part overlaps with the beginning of the *Gaia* time series, for which baseline data are available on one side only. These cuts ensure that the *Gaia* data contain both event and baseline information, which is required for any later comparison with *Gaia* astrometry. These cuts also remove alerts for which a single bright point or a poorly sampled excursion cannot distinguish microlensing from other forms of variability. A visual inspection of the rejected long-timescale tail did not reveal convincing microlensing candidates lost by this criterion. The sample was thereby reduced from 2665 to 513 alerts.

We did not impose a strict χ^2 threshold during this initial stage. A simple PSPL model can fit genuine events poorly when annual parallax, binary lens effects, binary source effects, or survey systematics are present. The purpose of the *Gaia*-only screening was therefore not to define the final sample but to select a manageable set of events for cross-matching, external-data collection, and detailed modelling.

3.2. Cross-matching, external photometry, and data preparation

The 513 preliminary candidates were cross-matched against external microlensing and transient surveys to identify previously recognised events and to assemble complementary photometry. We searched the alert and event lists of OGLE, KMTNet, MOA, ASAS-SN, ATLAS, and ZTF. This recovered counterparts to 64 OGLE, 69 KMTNet, 31 MOA, and 13 ZTF microlensing events within the *Gaia* DR4 time interval. These numbers are not mutually exclusive, as many events were detected by more than one survey.

We also cross-matched the candidates against catalogues of likely contaminants. These included young stellar objects (YSOs) from the *Gaia*–AllWISE and Konkoly Optical YSO catalogues (Marton et al. 2019, 2023), active galactic nuclei (AGN) and quasars from the Milliquas catalogue (Flesch 2023), *Gaia* DR3 variable AGN (Carnerero et al. 2023), nearby galaxies from GLADE+ (Dálya et al. 2022), and classified transients from the TNS (Gal-Yam 2021). These matches were used as vetting information rather than as automatic rejection criteria. Only clear non-microlensing contaminants were removed.

For events with available external data, we collected public photometry from KMTNet, MOA, and other survey pages (Kim et al. 2016; Bond et al. 2001). Although OGLE observations exist for several events in our sample, these data were not made available to us for this work. However, 53 of the 64 OGLE events were also monitored at high cadence by all three KMTNet telescopes, and therefore we do not expect the inclusion of the OGLE data to have significantly improved the constraints on the photometric light curves. These data were combined with follow-up observations available through the Black Hole Target and Observation Manager (BHTOM; Wyrzykowski 2024; Mikolajczyk et al. 2025), an observation-coordinating and data-processing server built on the open-source TOM Toolkit developed at Las Cumbres Observatory (Street et al. 2018, 2024). Each survey, observatory, and filter combination was treated as an independent dataset, so

that the microlensing model could assign separate source and blend fluxes to each photometric system. In a small number of very sparse BHTOM follow-up datasets, observations from different small telescopes were combined.

Before final modelling, we applied uniform cleaning cuts to all datasets. We retained only measurements with finite magnitudes and uncertainties, $\sigma_m < 0.2$ mag, and magnitudes in the range $0 < m < 22$. For each telescope and filter dataset separately, we calculated the median and standard deviation of the reported photometric uncertainties and removed measurements whose uncertainty exceeded the median by more than three standard deviations. For datasets containing more than 300 measurements, observations were grouped into one-day intervals. Within each bin, we calculated the inverse-variance weighted mean flux. The formal uncertainty of the binned flux was taken to be

$$\sigma_{\overline{F}} = \left(\sum_i \sigma_{F,i}^{-2} \right)^{-1/2} . \quad (4)$$

This procedure assumes that measurements within each daily bin are statistically independent. No additional correlated-noise model was included.

After cross-matching, external-data collection, and visual inspection of the light curves, we retained 229 vetted microlensing candidates. These candidates formed the final sample for parallax modelling.

3.3. Final PSPL modelling with and without annual parallax

For each vetted candidate we first fitted a blended PSPL model without parallax to the full multi-survey photometric dataset. We then repeated the fit with a blended PSPL model including annual microlensing parallax. Events whose light curves clearly required a different interpretation, such as binary-lens or binary-source models, or other non-PSPL behaviour, were excluded from the homogeneous sample.

The global optimisation was performed with the differential-evolution implementation in `pyLIMA` (Storn & Price 1997; Virtanen et al. 2020). The parameter ranges were chosen to be broad enough to include the *Gaia*-alert population while avoiding unphysical solutions. Annual microlensing parallax was included using the geocentric formalism implemented in `pyLIMA`. All datasets, including the *Gaia* photometry, were modelled in this geocentric frame; the effect of *Gaia*'s location at L2 is quantified in Sect. 4. The parallax model introduces the two components $\pi_{E,N}$ and $\pi_{E,E}$ of the microlensing-parallax vector. The event time t_0 was allowed to vary across the *Gaia* DR4 time interval ±100 days to avoid edge effects for long events. The impact parameter was restricted to $u_0 \in [-2, 2]$, the Einstein timescale to $t_E \in [5, 1000]$ d, and the parallax components to $\pi_{E,N}, \pi_{E,E} \in [-1, 1]$.

Posterior exploration was then carried out with the `pyLIMA` Markov chain Monte Carlo (MCMC) implementation (Foreman-Mackey et al. 2013) for both the blended PSPL and the combined blended PSPL and parallax models. The no-parallax solution provided the reference geometry and initial estimate of t_0 for the parallax fit. To explore the discrete degeneracies common in single-lens parallax modelling (Smith et al. 2003; Gould 2004), we initialised the parallax chains from multiple sign combinations of u_0, $\pi_{E,N}$, and $\pi_{E,E}$. In many events these initialisations converged to the same posterior mode, while in others multiple separated solutions remained viable. Solutions were treated as distinct only when the recovered parameters differed by more than their 1σ uncertainties in at least one of the microlensing parameters. Pure sign realisations that were statistically indistinguishable were not counted as separate physical solutions. Unless stated otherwise, the reported parameter estimates are the medians of the marginalised MCMC posteriors. The quoted 1σ uncertainties correspond to the 16th and 84th percentiles. For individual scalar parameters, a 3σ credible interval refers to the 0.135th to 99.865th percentile range.

3.4. Acceptance of parallax solutions

An event was retained in the final combined PSPL and parallax sample when the parallax solution satisfied three conditions. First, the parallax model had to provide a better fit than the corresponding no-parallax PSPL model. This was determined by comparing the χ^2 of each solution. Second, the MCMC posterior had to be bounded and not cut off by the parameter ranges. Third, the parallax vector had to be inconsistent with $\pi_E = 0$ at the 3σ level. We did not automatically reject formally negative blend fluxes. In heterogeneous aperture and survey photometry, the fitted blend term can absorb calibration offsets, unresolved background structure, or baseline mismatches. This can lead to negative blend parameters. The solutions for which this was the case were inspected and retained only when the overall microlensing interpretation remained plausible.

We excluded from the homogeneous sample events that had already been studied in other work. These studies include Gaia16aye (Wyrzykowski et al. 2020), Gaia18ajz (Howil et al. 2025), Gaia18cbf (Kruszyńska et al. 2022), Gaia19bld (Rybicki et al. 2022), Gaia19dke (Maskoliūnas et al. 2024), and the events from Rybicki et al. (2024) (Gaia18cej, Gaia18cho, Gaia19ayh, and Gaia19drv). Other events in the sample have been cross-matched with entries in other catalogues (e.g. Mróz et al. 2020; Medford et al. 2023); however, because they have not been studied extensively on an individual basis, they were retained in the sample.

4. Final photometric solutions

The final sample consists of 56 GSA microlensing events with 71 accepted PSPL and parallax solutions, whose sky positions are shown in Fig. 1. By construction, this is not a complete sample of *Gaia* microlensing alerts. The sample is biased towards events that are sufficiently well covered photometrically, that are long enough for annual parallax to be measurable, and that are adequately described by a single-lens model. These selection effects are appropriate for the goal of this work: to identify *Gaia*-alerted microlensing events for which pre-DR4 photometric mass predictions can be tested with future *Gaia* astrometry.

The fitted parameters for these solutions are listed in Tables A.1, A.2, and A.3, grouped by the year of the corresponding GSA alert. For each solution we report the event time t_0, impact parameter u_0, Einstein timescale t_E, parallax components $\pi_{E,N}$ and $\pi_{E,E}$, the *Gaia*-band source and blend flux parameters, and the χ^2/d.o.f.

The sample is dominated by moderately long events with measurable annual-parallax signatures. Figure 2 shows the distributions of the main microlensing parameters. The impact parameters are typically small, with a median $|u_0| = 0.15$, indicating that the final sample is biased towards relatively high-magnification events. The Einstein timescales span more than an order of magnitude and have a median $t_E \simeq 83$ days. Short events

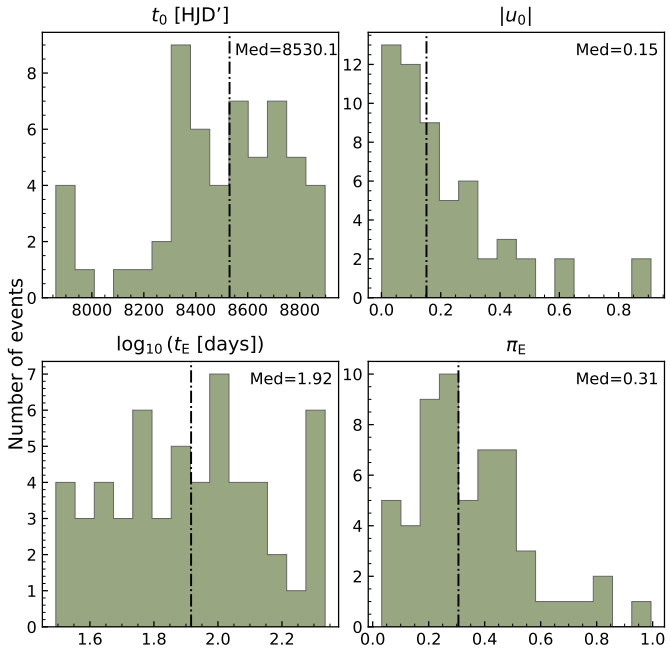

Fig. 2. Distribution of the best-model microlensing parameters for the final sample of events. The vertical dash-dotted lines with the corresponding 'Med' labels mark the median values of the distributions.

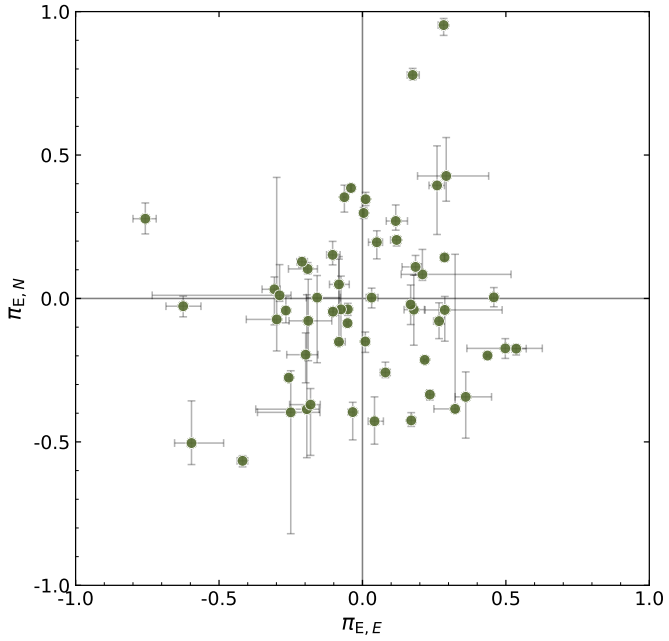

Fig. 3. Distribution of the best-model parallax parameters for the final sample of events. The parallax components, $\pi_{E,N}$ and $\pi_{E,E}$, represent the northern and eastern components, respectively.

are less likely to show measurable annual-parallax distortions and were therefore less likely to be retained in the sample.

The parallax amplitudes are shown in Fig. 2, and the corresponding vector components are shown in Fig. 3. The accepted solutions have a median $\pi_E = 0.31$ but cover a broad range of amplitudes and directions. The distribution of $(\pi_{E,N}, \pi_{E,E})$ is not expected to be isotropic as *Gaia* microlensing events are distributed across the sky. The distribution of microlens parallax amplitudes as a function of Einstein time is shown in Fig. 4. The largest parallax amplitudes ($\pi_E \gtrsim 0.6$) occur for $t_E \lesssim 130$ d, whereas all solutions with $t_E \gtrsim 200$ d have $\pi_E \lesssim 0.5$. For a given lens mass, the combination of a large π_E and a long t_E requires a nearby lens with an unusually low relative proper motion, and such events are rare. Conversely, all solutions with $t_E < 50$ d have $\pi_E > 0.15$, reflecting our requirement of a significant parallax detection (Sect. 3.4): short events show a measurable annual-parallax distortion only when π_E is large. Since $M_L = \theta_E/(\kappa\pi_E) = \mu_{rel} t_E/(\kappa\pi_E)$, events in the lower-right part of Fig. 4 (long t_E, small π_E) correspond to the most massive lenses for a given relative proper motion and are the natural candidates for massive or dark lenses.

Gaia observes from a Lissajous orbit around the Sun–Earth L2 point, at ≈0.01 au from the Earth. Because L2 lies on the Sun–Earth line, *Gaia*'s heliocentric trajectory differs from that of the Earth only by a radial scaling of ≈1.01 and by the Lissajous motion (≲0.005 au). For the annual-parallax signal this corresponds to a change of ≈1% in the effective π_E, well below the statistical uncertainties from the best model solutions. For an observer displaced by $D_\perp$ in the plane of the sky, the lens–source relative position shifts by $\pi_{rel} D_\perp$/au, i.e. by $\Delta u \simeq \pi_E D_\perp$/au in units of θ_E (Refsdal 1966; Gould 1994), where $D_\perp$ is the Earth–*Gaia* separation projected onto the sky. As Δu is a vector offset, it is an upper limit on the change in the scalar separation u. As shown in Fig. 5, the solutions closest to $\Delta u \approx |u_0|$ are high-magnification events; however, for the

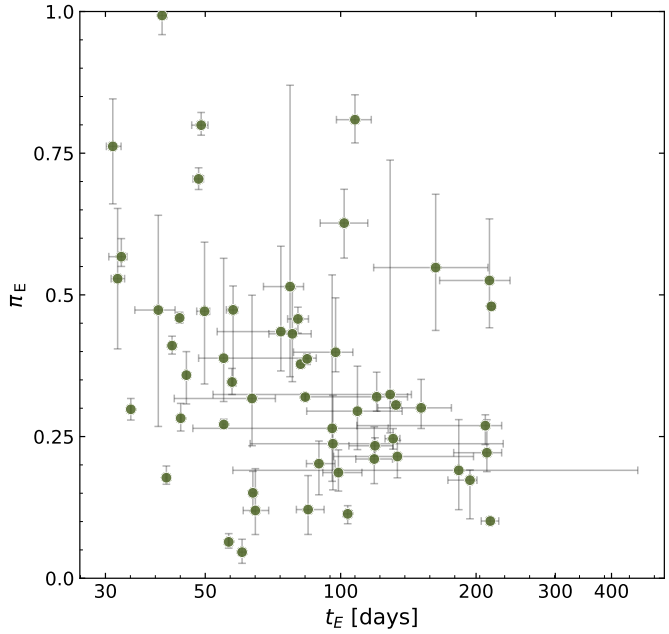

Fig. 4. Distribution of the best-model π_E parameters as a function of the Einstein time (t_E) for the final sample of events.

events in our sample, the nearest *Gaia* data epoch lies multiple days from t_0, where $u(t) \gg \Delta u$. The space parallax signal from *Gaia* is therefore not detected in the microlensing events in our sample. We therefore treated all datasets in the geocentric frame. A measurement of the Earth–L2 parallax requires dense *Gaia* and ground-based coverage close to the peak, as for the short-timescale planetary-mass event KMT-2024-BLG-0792/OGLE-2024-BLG-0516 (Dong et al. 2026), and is best investigated on an event-by-event basis.

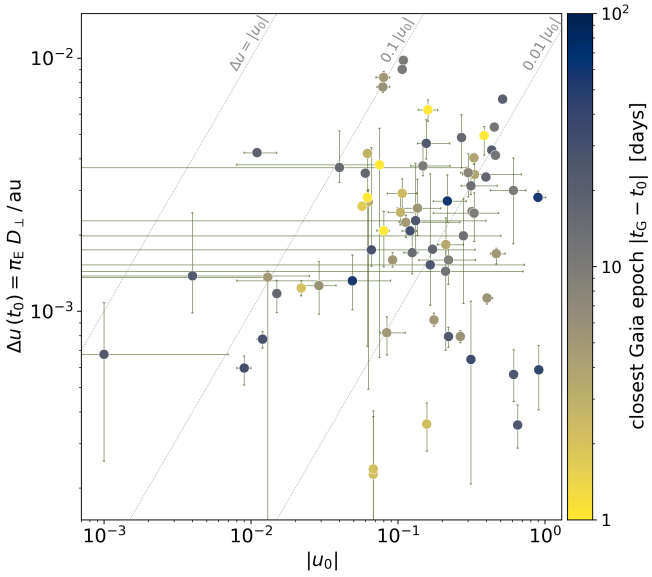

Fig. 5. Difference between the lens–source separations seen from the Earth and from *Gaia* at L2, $\Delta u(t_0) = \pi_E D_\perp$/au, as a function of $|u_0|$ for the microlensing events in this study. $D_\perp$ is the projected Earth–*Gaia* separation at t_0. The diagonal dotted lines mark $\Delta u = |u_0|$, $0.1|u_0|$ and $0.01|u_0|$. The colour scale shows the time between t_0 and the closest *Gaia* epoch, $|t_G - t_0|$.

5. *Gaia*-only versus all-data constraints

Gaia provides homogeneous all-sky discovery photometry, but its sampling is determined by the scanning law and is substantially sparser than that of dedicated ground-based microlensing surveys. The nominal *Gaia* scanning law provides approximately 70 focal-plane transits per source over five years, corresponding to an average of about one transit every 26 days, although the observations are distributed non-uniformly and may occur in closely spaced groups (Gaia Collaboration 2016).

This can limit the recovery of higher-order effects, in particular annual parallax. To quantify the role of follow-up photometry, we compared the PSPL and parallax solutions obtained from the full photometric datasets with corresponding fits that used only the *Gaia* *G*-band alert light curves. Both sets of fits used the same geocentric formalism. As the Earth–L2 effects are at the per-cent level in π_E (Sect. 4), the differences discussed below reflect the *Gaia* sampling rather than the observer location.

For each of the 71 accepted full-data solutions associated with 56 unique events, we performed a *Gaia*-only refit using the same model family, parameter bounds, and blending treatment as in Sect. 3. The MCMC chains were initialised from the corresponding best-fitting full-data solution. This setup tests whether the *Gaia* data can sustain a known solution once initialised near it, rather than whether a blind *Gaia*-only search would independently recover the same solution. In total, 51 of the 71 *Gaia*-only fits converge to physically acceptable solutions, corresponding to 41 of the 56 unique events. The remaining fits either fail to converge to a stable solution or yield posteriors that are not sufficiently constrained by the *Gaia* data alone. Among the 51 acceptable *Gaia*-only solutions, eight have parallax amplitudes consistent with $\pi_E = 0$ at the 1σ level. A non-zero *Gaia*-only parallax solution does not necessarily imply recovery of the full-data event geometry. Only 21 of the 51 acceptable *Gaia*-only solutions recover all three microlensing parameters within their 1σ uncertainty intervals. The individual parameters for u_0, t_E, and π_E are recovered in only 31, 29, and 37 cases, respectively. The relatively high recovery fraction for π_E should be interpreted with caution, because in many cases it is driven by broad uncertainty intervals rather than by a precise parallax measurement.

Figure 6 illustrates this behaviour. The impact parameter u_0 is the most robustly recovered of the three quantities, although several outliers remain. The Einstein timescale t_E shows larger scatter, with some *Gaia*-only solutions drifting towards substantially different values from those preferred by the full dataset. The strongest degradation is seen for the parallax amplitude $|\pi_E|$, where *Gaia*-only solutions are frequently broad, scattered, or displaced from the one-to-one relation. Thus, even when a *Gaia*-only PSPL fit with parallax formally converges, it often does not recover the same higher-order geometry as the combined *Gaia* and follow-up solution.

This shows that the physical interpretation of GSA microlensing events strongly depends on complementary photometric coverage. *Gaia* provides the all-sky discovery channel and, in DR4, the astrometric time series against which these events can be tested. However, dense ground-based photometry is usually required to constrain the photometric model and to obtain the parallax constraints needed for lens mass predictions.

6. Lens mass inference from photometric solutions

Although we extracted the microlensing parallax vector π_E from the photometric models, a direct mass measurement requires the angular Einstein radius θ_E. *Gaia* DR4 astrometric microlensing models will provide constraints on θ_E for the most favourable events, such that the mass can be determined. Before such astrometric information is available, the lens mass and distance must be inferred statistically by combining the photometric microlensing parameters with Galactic-population priors and source constraints.

We estimated lens properties using two independent approaches. First, we used `pyLIMASS` (Bachelet et al. 2024), which combines microlensing observables with stellar-population and isochrone information to infer posterior distributions for the physical lens parameters. Second, we used the approach of Shin et al. (2019) and Bachelet et al. (2022) based on the Besançon Galaxy Model (BGM) (Robin et al. 2003; Czekaj et al. 2014), in which simulated lens–source populations along the event line of sight are weighted by their consistency with the measured microlensing parameters.

For each accepted photometric solution, both methods were run in two configurations. In the first configuration, labelled *pyL* or *BGM*, we used only the photometric microlensing constraints and *Gaia*-band flux information. In the second configuration, labelled *pyL*+D_S or *BGM*+D_S, we additionally imposed a source-distance prior. This prior was taken from the photogeometric distance estimate of the corresponding *Gaia* source in the Bailer-Jones et al. (2021) catalogue.

The event Gaia19ect should be interpreted with caution. Its *Gaia* alert light curve shows two apparent baseline levels, near $G \simeq 19.5$ mag and $G \simeq 20.0$ mag, suggesting possible source variability, contamination, or source confusion in the *Gaia* photometry. We retained Gaia19ect in the sample because *Gaia* DR4 will provide an updated and longer *Gaia* time series, which may clarify the origin of the *Gaia* baseline offset.

The inferred lens masses and distances are reported in Tables B.1, B.2, and B.3, grouped by *Gaia* alert year. Figure 7 shows the resulting lens mass distributions, and Fig. 8 shows

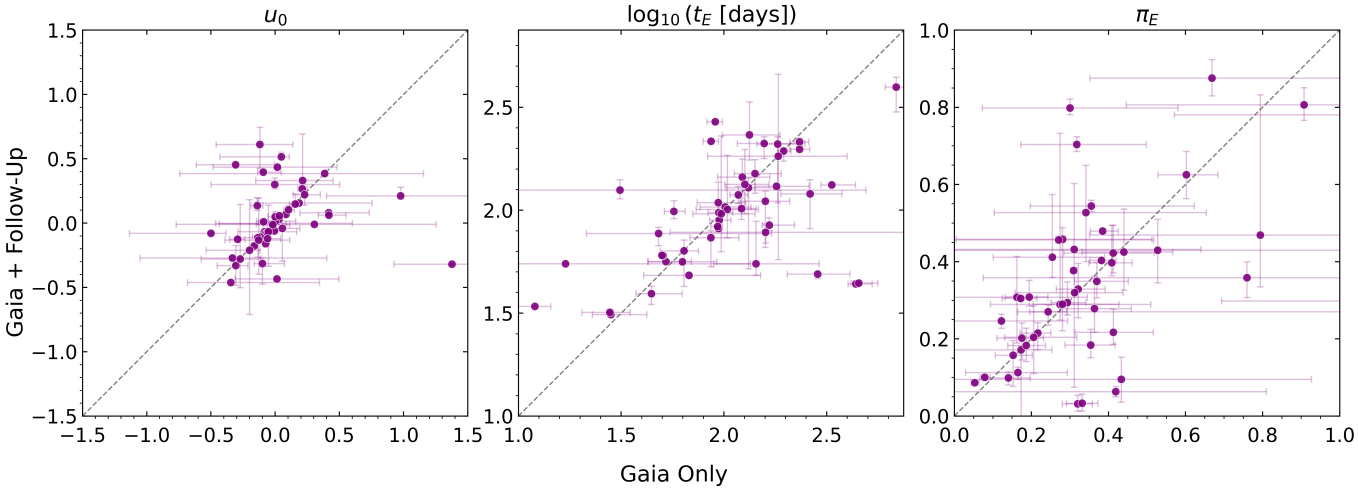

Fig. 6. Comparison of the parameters recovered from *Gaia*-only refits and from the corresponding *Gaia* and follow-up solutions for the subset of *Gaia*-only runs that converge to physically acceptable solutions. The dashed lines indicate equality. While u_0 is often recovered approximately, the scatter increases for t_E and becomes most pronounced for the parallax amplitude (π_E), illustrating the importance of complementary follow-up data for constraining higher-order microlensing parameters.

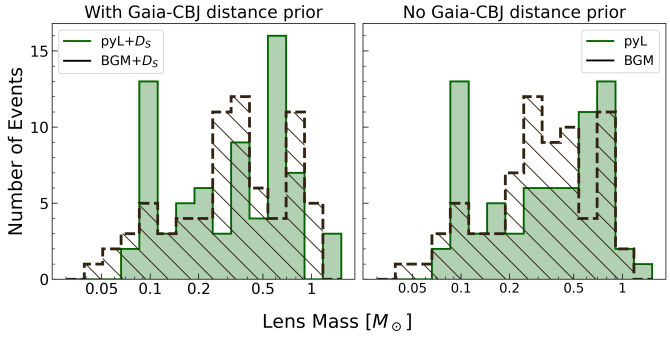

Fig. 7. Lens mass distributions inferred with `pyLIMASS` and the BGM-based Galactic-prior approach. Left panels: results obtained with the *Gaia* source-distance prior. Right panels: corresponding results without this prior.

the derived lens mass–distance distributions. Figure 9 shows the projected lens positions in the Galactic plane. The spread between the four configurations illustrates the dominant role of population and source-distance priors when θ_E is not yet measured.

None of the inferred lens masses significantly exceeds $\sim 1.5\,M_\odot$. This is largely a consequence of the inference method: without θ_E, the mass posterior is dominated by the Galactic and stellar-population priors, in which stellar remnants, and in particular neutron stars and black holes, carry little or no weight, while the lens-flux constraints further disfavour massive luminous lenses. The sample selection also contributes, as the best-studied long-timescale dark-lens candidates among the *Gaia* alerts (e.g. Gaia18cbf and Gaia18ajz) were excluded from the homogeneous sample. Events with long t_E and small π_E, such as Gaia17bdk, Gaia18bmt, Gaia18cik, and Gaia18dif, nevertheless, remain viable candidates for more massive or dark lenses. Because $\theta_E = \kappa M_L \pi_E$, a lens more massive than predicted would produce a proportionally larger astrometric signal, so our DR4 detectability estimates (Sect. 7) are conservative for such lenses, and a *Gaia* DR4 measurement of θ_E can directly test whether the prior-based masses are underestimated.

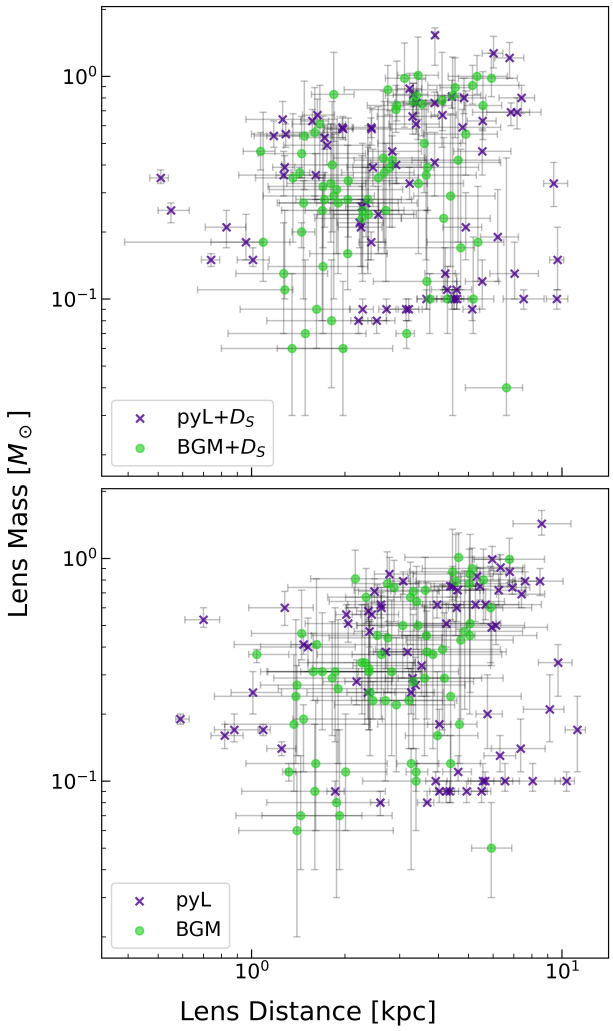

Fig. 8. Lens mass and distance distributions inferred with `pyLIMASS` and the BGM-based Galactic-prior approach. Top panels: results obtained with the *Gaia* source-distance prior. Bottom panels: corresponding results without this prior.

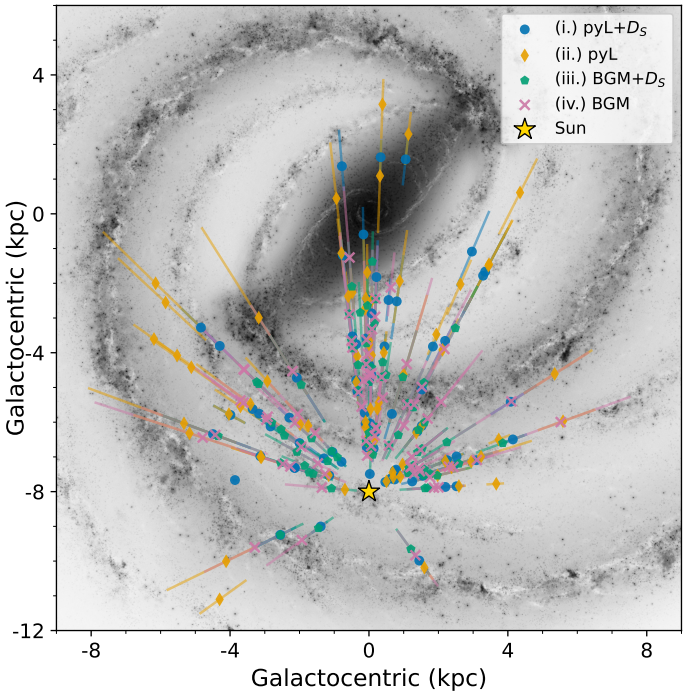

Fig. 9. Galactic projection of lens distances inferred with `pyLIMASS` and the BGM-based Galactic-prior approach. The blue circles and orange diamonds show the lens distance for the `pyLIMASS` solution where the *Gaia* source-distance prior was and was not used, respectively. The green pentagon and pink 'x' display the lens distance for the `BGM`-based Galactic-prior solution with and without the *Gaia* source-distance prior, respectively. The figure was made using `MW-Plot` and *Gaia* EDR3 data (Gaia Collaboration 2021).

7. Predicted astrometric microlensing signals for *Gaia* DR4

The lens mass posteriors from Sect. 6 allow us to predict the astrometric microlensing signal expected in *Gaia* DR4. We simulated the astrometric signals using the `astromet`[4] package (Penoyre et al. 2022). For each event, the photometric microlensing parameters were combined with the *Gaia* DR3 five-parameter astrometric solution, the angular Einstein radius, θ_E, inferred from the lens parameters, and the event-specific *Gaia* scanning law over the DR4 time interval. We used the `Gaia Observation Forecast Tool`[5] to determine *Gaia* focal-plane crossing times. We then generated *Gaia*-like along-scan (AL) astrometric measurements for the predicted lensed trajectory. The same simulated data were fitted with a standard five-parameter astrometric model, including position, parallax, and proper motion only. To test whether the *Gaia* DR4 astrometric time series expected for a known photometric microlensing event should be better described by a standard single-source astrometric solution or by an astrometric microlensing model, we additionally fitted a model extended to include the astrometric microlensing signal.

Uncertainties in the photometric and lens-prior inputs were propagated by Monte Carlo sampling. For each draw, we generated a new astrometric microlensing realisation, simulated the corresponding *Gaia* AL observations, and refitted both the standard five-parameter and microlensing astrometric models.

[4] https://github.com/zpenoyre/astromet.py
[5] https://gaia.esac.esa.int/gost/

A major source of confusion in astrometric microlensing is light from the lens or from unrelated blends within the *Gaia* window. For a luminous lens with blend-to-source flux ratio $g := f_b/f_s$, the centroid shift relative to the unlensed source position becomes $\delta\theta = \theta_E\, u\,[A/(u^2+2) - g]/(A+g)$. This reduces to the dark-lens expression $\theta_E u/(u^2+2)$ for $g = 0$ (e.g. Dominik & Sahu 2000; Jeong et al. 1999). Lens light therefore reduces the amplitude of the shift, alters the shape of the astrometric trajectory, and introduces a term following the lens–source relative motion that can be partly absorbed by the five-parameter solution. Joint fits to the *Gaia* DR4 epoch photometry and astrometry constrain the lens flux directly, allowing dark and luminous lenses to be distinguished. Because light from an unrelated blend does not follow the lens–source relative motion, its astrometric signature differs from that of a luminous lens. Joint fits can therefore help to establish the nature of the lens and to identify cases in which an additional, unrelated blend must be included in the model.

We quantified the detectability of an astrometric signal in *Gaia* DR4 using the Bayesian information criterion improvement, $\Delta\mathrm{BIC} = \mathrm{BIC}_{5p} - \mathrm{BIC}_{5p+\mathrm{ML}}$. Positive values indicate that the BIC favours the astrometric-microlensing model over the standard five-parameter (5p) model.

Out of the 284 mass-distance branches derived for the 56 events, we classified 47 branches as high-confidence detections with $\Delta\mathrm{BIC} > 10$ and $S/N_{\theta_E} > 3$. These 47 branches correspond to the following 17 events: Gaia18ajt, Gaia18akb, Gaia18bmt, Gaia18ceb, Gaia18ces, Gaia18cgp, Gaia18cjk, Gaia18cov, Gaia18dep, Gaia18dif, Gaia19aqw, Gaia19bcm, Gaia19bii, Gaia19chi, Gaia19dae, Gaia19dtd, and Gaia19eca. An additional 18 branches have $\Delta\mathrm{BIC} > 5$ and $S/N_{\theta_E} > 3$ and a total of 72 branches have $\Delta\mathrm{BIC} > 3$ and $S/N_{\theta_E} > 3$, which includes the events Gaia18cib, Gaia18cnm, Gaia19eim, and Gaia19eku. For these 72 branches, 61% (44 branches) recover the injected θ_E value within 1σ.

Combining a *Gaia* DR4 measurement of θ_E with the photometric π_E yields the lens mass directly, $M_L = \theta_E/(\kappa\pi_E)$. For the 17 events with high-confidence branches, the photometric π_E is measured with fractional uncertainties of $< 30\%$, with the exception of Gaia18bmt. To quantify the expected precision, we propagated, for each simulated realisation, the recovered θ_E and its uncertainty together with the photometric π_E posterior of the corresponding branch. The median fractional lens mass uncertainty is 24%. Since these branches satisfy $S/N_{\theta_E} > 3$, the uncertainty on θ_E dominates the mass error budget for most events. The expected precision improves for brighter sources with larger S/N_{θ_E} (Fig. 10). The lens distance, $D_L = \mathrm{au}/(\pi_{rel} + \pi_S)$ with $\pi_{rel} = \theta_E\pi_E$, additionally depends on the source parallax π_S, which will be determined directly by joint fits with *Gaia* DR4 astrometry. Additionally, the astrometric trajectory constrains the direction of $\boldsymbol{\mu}_{rel}$, which must be parallel to $\boldsymbol{\pi}_E$. This provides a consistency test of the photometric solution and a means to break discrete degeneracies, such as those between solutions with opposite signs of u_0.

We show in Fig. 10 that the strength of an astrometric signal heavily depends on the brightness of the source. An effective *Gaia* magnitude limit for astrometric microlensing is not fixed, as it also depends on the angular Einstein radius, event duration, and scanning-law coverage. Astrometric microlensing signals can still be recovered for faint sources when the event has a large angular Einstein radius, θ_E (Jankovič et al. 2025).

In Fig. 11 we show the light curve and simulated astrometric tracks for Gaia19bcm using the *pyL+D*$_S$ solution with the source-distance prior. Because *Gaia* provides 1D AL astrometric

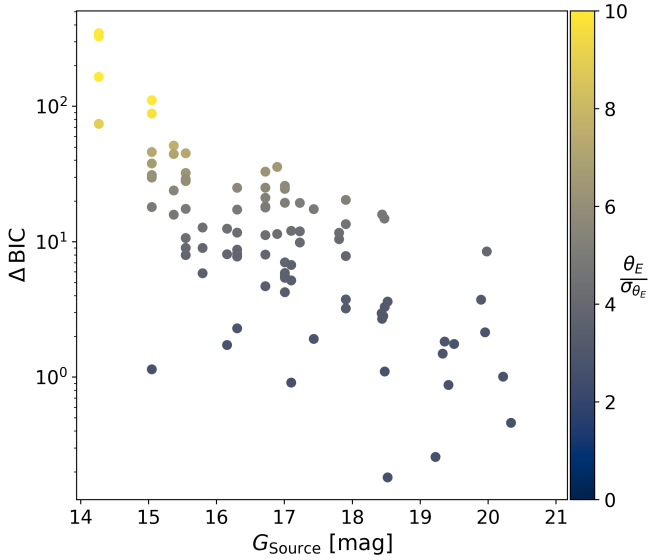

Fig. 10. Strength of astrometric microlensing signal as a function of the *Gaia* DR3 G-band magnitude. The colour bar shows the signal-to-noise ratio of the angular Einstein radius.

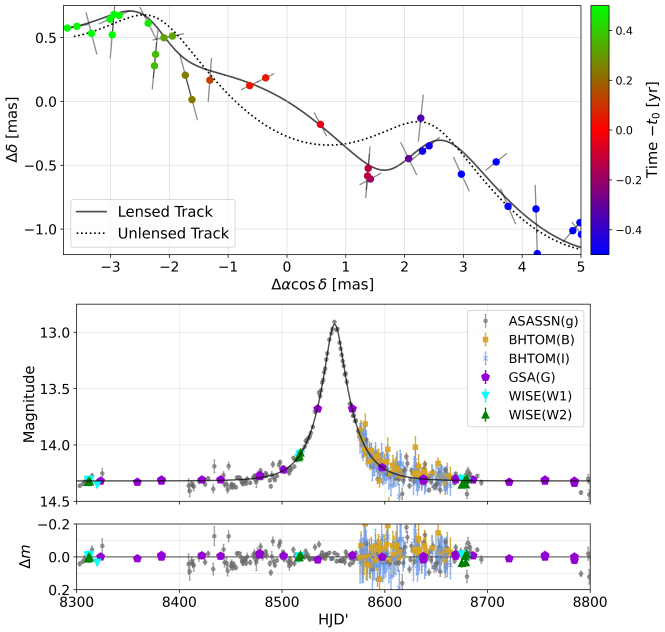

Fig. 11. Observed and modelled light curve (bottom) and simulated astrometric track (top) for the Gaia19bcm microlensing event. The astrometric track was simulated for solutions assuming lens parameters from the pyL+D_S solution. The solid line marks the astrometric track due to the microlensing event. The coloured dots mark the simulated *Gaia* DR4 AL light centroids from the *Gaia* scanning laws. The dashed line marks the best 5p-fit for the data points. The light curve shows the combined *Gaia* and follow-up data as well as the combined PSPL and parallax model with parameters from Table A.3.

measurements, we show the simulated astrometric residuals from the 5p fits with and without microlensing in Fig. 12.

Overall, these results indicate that a non-negligible subset of GSA photometric microlensing events should produce detectable astrometric perturbations in *Gaia* DR4-like data. The most significant cases provide both a statistically preferred astrometric microlensing solution and a meaningful recovery of $\theta_{\rm E}$.

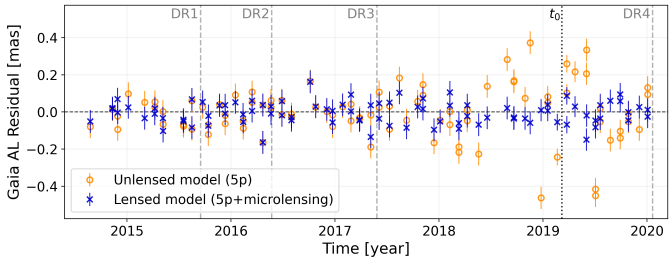

Fig. 12. Simulated *Gaia* AL astrometric residuals for Gaia19bcm, assuming lens parameters from the pyL + D_S solution. The open orange circles show the residuals obtained after fitting a standard five-parameter (5p) astrometric model, while the blue crosses show the residuals obtained with a five-parameter model including astrometric microlensing. The error bars indicate the adopted single-epoch AL uncertainties, and the horizontal dashed line marks the zero residual. The vertical dashed grey lines mark the temporal limits associated with *Gaia* DR1, DR2, DR3, and DR4, while the dotted black line indicates t_0 from the microlensing model.

This makes them good candidates for combining *Gaia* astrometry with existing photometric microlensing constraints to infer physical lens properties.

8. Conclusions

We constructed a pre-DR4 benchmark sample of GSA microlensing events for which forthcoming *Gaia* astrometry will be available. The epoch astrometry data in *Gaia* DR4 can test the photometric microlensing models as well as predicted lens masses and distances. The GSA archive, constrained to alerts issued before the *Gaia* DR4 time cut, provided our parent sample of 11 048 light curves. We first identified candidate microlensing events through *Gaia*-only PSPL screening, cross-matching with external microlensing and contaminant catalogues, and visual inspection of the *Gaia* and follow-up light curves. We then performed homogeneous blended PSPL and parallax modelling and retained events for which the photometry supports a non-zero parallax signal. The final sample contains 56 events with 71 accepted PSPL and parallax solutions.

The comparison in Fig. 6 shows that follow-up photometry is vital for the recovery of the microlensing parameters. *Gaia* provides an all-sky discovery channel and identifies events that are highly valuable for later astrometric verification, but dense external photometry is often required to constrain the photometric solution and to recover physical parameters. This remains an important part of microlensing detections for the LSST (Ivezić et al. 2019) alert stream. Despite a median inter-night cadence of approximately three days in the Wide–Fast–Deep survey, coordinated follow-up and cross-survey photometry will still be required for the robust classification and modelling of microlensing events (Abrams et al. 2025). Spectroscopic follow-up, even after the microlensing event has ended, provides complementary constraints by improving the characterisation of the source star. These include constraints on its effective temperature, surface gravity, metallicity, and distance, which can in turn strengthen the inference of the physical lens properties.

Using `pyLIMASS` and a BGM-based Galactic-prior framework, we derived lens mass and distance predictions for each accepted photometric solution. The differences between the inference configurations show that, without a direct measurement of $\theta_{\rm E}$, the inferred lens properties remain strongly prior-dependent. Our *Gaia* DR4-like simulations predict that 47

event–solution branches should be high-confidence astrometric detections, with a further 25 potentially detectable cases. This motivates the use of *Gaia* DR4 astrometry, and other complementary constraints, to turn these photometric predictions into physical lens measurements.

Acknowledgements. BHTOM.space is based on the open-source TOM Toolkit by LCO and has been developed with funding from the OPTICON-RadioNet Pilot (ORP) of the European Union's Horizon 2020 research and innovation programme under grant agreement No. 101004719 (2021–2025). This project has received funding from the European Union's Horizon Europe Research and Innovation programme ACME under grant agreement No. 101131928 (2024–2028). Ł.W. acknowledges support from the Polish National Science Centre DAINA grant No. 2024/52/L/ST9/00210. E.S., M.M., E.P., J.Z., V.C., and U.J. acknowledge funding from the Research Council of Lithuania (LMTLT, grant No. S-LL-24-1). This work makes use of observations from the Las Cumbres Observatory global telescope network. This work has made use of data from the European Space Agency (ESA) mission *Gaia* (https://www.cosmos.esa.int/gaia), processed by the *Gaia* Data Processing and Analysis Consortium (DPAC; https://www.cosmos.esa.int/web/gaia/dpac/consortium). Funding for DPAC has been provided by national institutions, in particular the institutions participating in the *Gaia* Multilateral Agreement. This research has made use of publicly available data (https://kmtnet.kasi.re.kr/ulens/) from the KMTNet system operated by the Korea Astronomy and Space Science Institute (KASI) at three host sites of CTIO in Chile, SAAO in South Africa, and SSO in Australia. Data transfer from the host site to KASI was supported by the Korea Research Environment Open NETwork (KREONET). This paper makes use of data obtained by the MOA collaboration with the 1.8-metre MOA-II telescope at the University of Canterbury Mount John Observatory, Lake Tekapo, New Zealand. The MOA project is supported by JSPS KAKENHI Grant Number JP16H06287, JP22H00153, JP23KK0060 and JP25H00668. These data are made available using services at the NASA Exoplanet Archive, which is operated by the California Institute of Technology, under contract with the National Aeronautics and Space Administration under the Exoplanet Exploration Program. This work makes use of observations obtained with the Samuel Oschin Telescope 48-inch and the 60-inch Telescope at the Palomar Observatory as part of the Zwicky Transient Facility project. ZTF is supported by the National Science Foundation under Award 2407588 and a partnership including Caltech, USA; Caltech/IPAC, USA; University of Maryland, USA; University of California, Berkeley, USA; University of Wisconsin at Milwaukee, USA; Cornell University, USA; Drexel University, USA; University of North Carolina at Chapel Hill, USA; Institute of Science and Technology, Austria; National Central University, Taiwan; and OKC, University of Stockholm, Sweden. Operations are conducted by Caltech's Optical Observatory (COO), Caltech/IPAC, and the University of Washington at Seattle, USA. J.M.C. was (partially) supported by the Spanish MICIN/AEI/10.13039/501100011033 and by "ERDF A way of making Europe" by the "European Union" through grant PID2021-122842OB-C21 and PID2024-157964OB-C21, and the Institute of Cosmos Sciences University of Barcelona (ICCUB, Unidad de Excelencia 'María de Maeztu') through grant CEX2024-001451-M and the project 2021-SGR-00679 GRC de l'Agència de Gestió d'Ajuts Universitaris i de Recerca (Generalitat de Catalunya). The Joan Oró Telescope (TJO) of the Montsec Observatory (OdM) is owned by the Catalan Government and operated by the Institute for Space Studies of Catalonia (IEEC). H.H.E. thanks the Türkiye National Observatories for partial support in using the TUG-T100 telescope under project number 15CT100-915. M.W. thanks M.J. Mróz for his collaboration and feedback.

References

Abrams, N. S., Hundertmark, M. P. G., Khakpash, S., et al. 2025, ApJS, 276, 10
Alcock, C., Akerlof, C. W., Allsman, R. A., et al. 1993, Nature, 365, 621
Aubourg, E., Bareyre, P., Bréhin, S., et al. 1993, Nature, 365, 623
Bachelet, E., Norbury, M., Bozza, V., & Street, R. 2017, AJ, 154, 203
Bachelet, E., Tsapras, Y., Gould, A., et al. 2022, AJ, 164, 75
Bachelet, E., Hundertmark, M., & Calchi Novati, S. 2024, AJ, 168, 24
Bailer-Jones, C. A. L., Rybizki, J., Fouesneau, M., Demleitner, M., & Andrae, R. 2021, AJ, 161, 147
Ban, M., Voloshyn, P., Adomavičienė, R., et al. 2025, A&A, 697, A57
Bellm, E. C., Kulkarni, S. R., Graham, M. J., et al. 2019, PASP, 131, 018002
Belokurov, V. A., & Evans, N. W. 2002, MNRAS, 331, 649
Bond, I. A., Abe, F., Dodd, R. J., et al. 2001, MNRAS, 327, 868
Brown, T. M., Baliber, N., Bianco, F. B., et al. 2013, PASP, 125, 1031
Carnerero, M. I., Raiteri, C. M., Rimoldini, L., et al. 2023, A&A, 674, A24
Czekaj, M. A., Robin, A. C., Figueras, F., Luri, X., & Haywood, M. 2014, A&A, 564, A102
Dálya, G., Díaz, R., Bouchet, F. R., et al. 2022, MNRAS, 514, 1403
Domènech Rams, G., Herrero, K., Gil, P., Baroch, D., & Domene, F. 2025, in EPSC-DPS Joint Meeting 2025, 2025, EPSC-DPS2025-1736
Dominik, M., & Sahu, K. C. 2000, ApJ, 534, 213
Dong, S., Wu, Z., Ryu, Y.-H., et al. 2026, Science, 391, 96
Flesch, E. W. 2023, Open J. Astrophys., 6, 49
Foreman-Mackey, D., Hogg, D. W., Lang, D., & Goodman, J. 2013, PASP, 125, 306
Gaia Collaboration (Prusti, T., et al.) 2016, A&A, 595, A1
Gaia Collaboration (Brown, A. G. A., et al.) 2021, A&A, 649, A1
Gal-Yam, A. 2021, in American Astronomical Society Meeting Abstracts, 237, 423.05
Gould, A. 1994, ApJ, 421, L75
Gould, A. 2000, ApJ, 542, 785
Gould, A. 2004, ApJ, 606, 319
Hardy, L. K., Butterley, T., Dhillon, V. S., Littlefair, S. P., & Wilson, R. W. 2015, MNRAS, 454, 4316
Harris, M., Dragomir, D., Bachelet, E., Fausnaugh, M., & Johnson, S. 2026, ApJ, 1005, L33
Hodgkin, S. T., Harrison, D. L., Breedt, E., et al. 2021, A&A, 652, A76
Howil, K., Wyrzykowski, Ł., Kruszyńska, K., et al. 2025, A&A, 694, A94
Ivezić, Ž., Kahn, S. M., Tyson, J. A., et al. 2019, ApJ, 873, 111
Jabłońska, M., Wyrzykowski, Ł., Rybicki, K. A., et al. 2022, A&A, 666, L16
Jankovič, T., Gomboc, A., Wyrzykowski, Ł., et al. 2025, A&A, 699, A156
Jeong, Y., Han, C., & Park, S.-H. 1999, ApJ, 511, 569
Kim, S.-L., Lee, C.-U., Park, B.-G., et al. 2016, J. Korean Astron. Soc., 49, 37
Kruszyńska, K., Wyrzykowski, Ł., Rybicki, K. A., et al. 2022, A&A, 662, A59
Kruszyńska, K., Wyrzykowski, Ł., Rybicki, K. A., et al. 2024, A&A, 692, A28
Levenberg, K. 1944, Q. Appl. Math., 2, 164
Marquardt, D. W. 1963, J. Soc. Ind. Appl. Math., 11, 431
Marton, G., Ábrahám, P., Szegedi-Elek, E., et al. 2019, MNRAS, 487, 2522
Marton, G., Ábrahám, P., Rimoldini, L., et al. 2023, A&A, 674, A21
Maskoliūnas, M., Wyrzykowski, Ł., Howil, K., et al. 2024, Acta Astron., 74, 77
Medford, M. S., Abrams, N. S., Lu, J. R., Nugent, P., & Lam, C. Y. 2023, ApJ, 947, 24
Mikolajczyk, P. J., Zieliński, P., Wyrzykowski, Ł., Krawczyk, A., & Kotysz, K. 2025, in Revista Mexicana de Astronomia y Astrofisica Conference Series, 59, 167
Minniti, D., Lucas, P. W., Emerson, J. P., et al. 2010, New A, 15, 433
Mróz, P., Udalski, A., Szymański, M. K., et al. 2020, ApJS, 249, 16
Paczyński, B. 1986, ApJ, 304, 1
Penny, M. T., Gaudi, B. S., Kerins, E., et al. 2019, ApJS, 241, 3
Penoyre, Z., Belokurov, V., & Evans, N. W. 2022, MNRAS, 513, 2437
Refsdal, S. 1966, MNRAS, 134, 315
Reichart, D., Nysewander, M., Moran, J., et al. 2005, Nuovo Cimento C Geophys. Space Phys. C, 28, 767
Robin, A. C., Reylé, C., Derrière, S., & Picaud, S. 2003, A&A, 409, 523
Rybicki, K. A., Wyrzykowski, Ł., Klencki, J., et al. 2018, MNRAS, 476, 2013
Rybicki, K. A., Wyrzykowski, Ł., Bachelet, E., et al. 2022, A&A, 657, A18
Rybicki, K. A., Shvartzvald, Y., Yee, J. C., et al. 2024, ApJ, 975, 216
Sahu, K. C., Anderson, J., Casertano, S., et al. 2022, ApJ, 933, 83
Shappee, B., Prieto, J., Stanek, K. Z., et al. 2014, in American Astronomical Society Meeting Abstracts, 223, 236.03
Shin, I.-G., Yee, J. C., Gould, A., et al. 2019, AJ, 158, 199
Smith, M. C., Mao, S., & Paczyński, B. 2003, MNRAS, 339, 925
Storn, R., & Price, K. 1997, J. Global Optim., 11, 341
Street, R. A., Bowman, M., Saunders, E. S., & Boroson, T. 2018, SPIE Conf. Ser., 10707, 1070711
Street, R. A., Lindstrom, W., Heinrich-Josties, E., et al. 2024, in Astronomical Society of the Pacific Conference Series, 535, Astronomical Data Analysis Software and Systems XXXI, eds. B. V. Hugo, R. Van Rooyen, & O. M. Smirnov, 3
Štrobl, J., Jelínek, M., Polášek, C., & Hudec, R. 2023, Contrib. Astron. Observ. Skalnate Pleso, 53, 49
Sumi, T., Buckley, D. A. H., Kutyrev, A. S., et al. 2025, AJ, 170, 338
Tonry, J. L., Denneau, L., Heinze, A. N., et al. 2018, PASP, 130, 064505
Udalski, A., Szymanski, M., Kaluzny, J., et al. 1993, Acta Astron., 43, 289
Udalski, A., Szymański, M. K., & Szymański, G. 2015, Acta Astron., 65, 1
Virtanen, P., Gommers, R., Oliphant, T. E., et al. 2020, Nat. Methods, 17, 261
Wicker, M., Wyrzykowski, Ł., Hundertmark, M., et al. 2026, A&A, 710, A294
Wu, Z., Dong, S., Yi, T., et al. 2024, AJ, 168, 62
Wyrzykowski, Ł. 2024, in What Was That? – Planning ESO Follow up for Transients, Variables, and Solar System Objects in the Era of LSST, 4
Wyrzykowski, Ł., Mróz, P., Rybicki, K. A., et al. 2020, A&A, 633, A98
Wyrzykowski, Ł., Kruszyńska, K., Rybicki, K. A., et al. 2023, A&A, 674, A23

Xilouris, E. M., Basilakos, S., & Marousis, A. 2025, SPIE Conf. Ser., 13699, 136993E
Zerbi, F. M., Chincarini, G., Ghisellini, G., et al. 2004, SPIE Conf. Ser., 5492, 1590

[1] Astronomical Observatory, University of Warsaw, Al. Ujazdowskie 4, 00-478 Warsaw, Poland
[2] Isaac Newton Group of Telescopes, Apartado 321, 38700 Santa Cruz de La Palma, Spain
[3] Astrophysics Division, National Centre for Nuclear Research, Pasteura 7, 02-093 Warsaw, Poland
[4] Astronomisches Rechen-Institut, Zentrum für Astronomie der Universität Heidelberg (ZAH), Mönchhofstr. 12–14, 69120 Heidelberg, Germany
[5] Las Cumbres Observatory, 6740 Cortona Drive, Suite 102, Goleta, CA 93117, USA
[6] Université Marie et Louis Pasteur, CNRS, Institut UTINAM UMR 6213, Besançon, France
[7] Institute of Astronomy, Faculty of Physics, Astronomy and Informatics, Nicolaus Copernicus University, Grudziądzka 5, 87-100 Toruń, Poland
[8] Astronomical Institute, University of Wrocław, ul. Mikołaja Kopernika 11, 51-622 Wrocław, Poland
[9] Research School of Astronomy and Astrophysics, Australian National University, Mount Stromlo Observatory, Cotter Road, Weston Creek, ACT 2611, Australia
[10] Vilnius University, Faculty of Physics, Institute of Theoretical Physics and Astronomy, Sauletekio av. 3, 10257 Vilnius, Lithuania
[11] Dipartimento di Fisica "E.R. Caianiello", Università di Salerno, Via Giovanni Paolo II 132, 84084 Fisciano, Italy
[12] Istituto Nazionale di Fisica Nucleare, Sezione di Napoli, Via Cintia, 80126 Napoli, Italy
[13] Institut d'Astrophysique de Paris, Sorbonne Université, CNRS, UMR 7095, 98 bis bd Arago, 75014 Paris, France
[14] University of St Andrews, School of Physics & Astronomy, St Andrews Centre for Exoplanet Science (StACES), North Haugh, St Andrews, KY16 9SS, UK
[15] Millennium Institute of Astrophysics MAS, Nuncio Monsenor Sotero Sanz 100, Of. 104, Providencia, Santiago, Chile
[16] Instituto de Astrofísica, Facultad de Física, Pontificia Universidad Católica de Chile, Av. Vicuña Mackenna 4860, 7820436 Macul, Santiago, Chile
[17] Departamento de Matemática y Física Aplicadas, Facultad de Ingeniería, Universidad Católica de la Santísima Concepción, Alonso de Rivera 2850, Concepción, Chile
[18] National Astronomical Research Institute of Thailand (Public Organization), 260 Moo 4, Donkaew, Mae Rim, Chiang Mai 50180, Thailand
[19] Centre for Advanced Instrumentation, Department of Physics, Durham University, South Road DH1 3LE, UK
[20] School of Physics, Trinity College Dublin, The University of Dublin, Dublin 2, Ireland
[21] Departament de Física Quàntica i Astrofísica (FQA), Universitat de Barcelona (UB), Martí i Franquès 1, 08028 Barcelona, Spain
[22] Institut de Ciències del Cosmos (ICCUB), Universitat de Barcelona (UB), Martí i Franquès 1, 08028 Barcelona, Spain
[23] Institut d'Estudis Espacials de Catalunya (IEEC), Edifici RDIT, Campus UPC, 08860 Castelldefels (Barcelona), Spain
[24] INAF Osservatorio di Astrofisica e Scienza dello Spazio di Bologna, via Piero Gobetti 93/3, 40129 Bologna, Italy
[25] Astrophysics Research Cluster, School of Mathematical and Physical Sciences, University of Sheffield, Sheffield S3 7RH, UK
[26] Instituto de Astrofísica de Canarias, 38205 La Laguna, Tenerife, Spain
[27] Istanbul University, Faculty of Science, Department of Astronomy and Space Sciences, 34119 Istanbul, Türkiye
[28] Astronomical Institute of the Academy of Sciences of the Czech Republic (ASU CAS), 25165 Ondrejov, Czech Republic
[29] Faulkes Telescope Project, Cardiff, Wales, UK
[30] The Schools' Observatory, Astrophysics Research Institute, Liverpool John Moores University, 146 Brownlow Hill, Liverpool, UK
[31] Department of Physics and Astronomy, University of Turku, 20014 Turku, Finland
[32] Finnish Centre for Astronomy with ESO (FINCA), 20014 University of Turku, Finland
[33] Université Côte d'Azur, CNRS, OCA, Lagrange, France
[34] Institute for Space-Earth Environmental Research, Nagoya University, Nagoya 464-8601, Japan
[35] Code 667, NASA Goddard Space Flight Center, Greenbelt, MD 20771, USA
[36] Department of Astronomy, University of Maryland, College Park, MD 20742, USA
[37] School of Mathematical and Computational Sciences, Massey University, Auckland 0745, New Zealand
[38] Department of Earth and Space Science, Graduate School of Science, The University of Osaka, Toyonaka, Osaka 560-0043, Japan
[39] Institute of Astronomy, Graduate School of Science, The University of Tokyo, 2-21-1 Osawa, Mitaka, Tokyo 181-0015, Japan
[40] Department of Physics, The Catholic University of America, Washington, DC 20064, USA
[41] Institute of Space and Astronautical Science, Japan Aerospace Exploration Agency, 3-1-1 Yoshinodai, Chuo, Sagamihara, Kanagawa 252-5210, Japan
[42] Department of Physics, University of Auckland, Private Bag 92019, Auckland, New Zealand
[43] College of Science and Engineering, Kanto Gakuin University, Yokohama, Kanagawa 236-8501, Japan
[44] University of Canterbury Mt. John Observatory, PO Box 56, Lake Tekapo 8770, New Zealand

Appendix A: Model parameters

Table A.1. Model parameters for GSA alerts from 2017.

Event	RA (°)	Dec (°)	t_0 (HJD')	u_0	t_E (days)	$\pi_{E,N}$	$\pi_{E,E}$	f_b/f_s	χ^2 / dof	Mod.
Gaia17aqu	116.0932	-28.4434	$7880.592^{+0.174}_{-0.155}$	$-0.080^{+0.008}_{-0.007}$	$89.47^{+7.69}_{-5.54}$	$0.196^{+0.040}_{-0.058}$	$0.050^{+0.020}_{-0.029}$	$0.15^{+0.14}_{-0.10}$	144.3 / 264	A
Gaia17bbs	272.7051	-22.6155	$7861.190^{+0.117}_{-0.592}$	$0.013^{+0.001}_{-0.022}$	$193.83^{+7.07}_{-20.72}$	$-0.151^{+0.288}_{-0.010}$	$-0.082^{+0.022}_{-0.010}$	$0.06^{+0.27}_{-0.22}$	42.0 / 92	A
Gaia17bdk	265.6345	-34.1037	$7878.511^{+0.003}_{-0.003}$	$0.157^{+0.001}_{-0.001}$	$56.38^{+0.12}_{-0.11}$	$-0.038^{+0.021}_{-0.021}$	$-0.051^{+0.007}_{-0.006}$	$0.00^{+0.01}_{-0.01}$	447.1 / 626	A
Gaia17bej	274.2544	-31.3835	$7875.220^{+0.080}_{-0.056}$	$0.029^{+0.009}_{-0.008}$	$118.76^{+11.65}_{-10.73}$	$-0.039^{+0.120}_{-0.124}$	$0.179^{+0.037}_{-0.034}$	$0.11^{+0.16}_{-0.15}$	157.4 / 199	A
Gaia17cah	268.9144	-31.3086	$7966.552^{+0.002}_{-0.002}$	$0.092^{+0.001}_{-0.001}$	$57.35^{+0.12}_{-0.12}$	$0.346^{+0.024}_{-0.022}$	$0.011^{+0.005}_{-0.007}$	$-0.05^{+0.01}_{-0.01}$	2076.9 / 3105	A

Notes. Microlensing model parameters are reported as $x^{+\sigma_+}_{-\sigma_-}$, with uncertainties corresponding to the 16th and 84th percentiles.

Table A.2. Model parameters for GSA alerts from 2018.

Event	RA (°)	Dec (°)	t_0 (HJD')	u_0	t_E (days)	$\pi_{E,N}$	$\pi_{E,E}$	f_b/f_s	χ^2 / dof	Mod.
Gaia18ajt	267.1333	-35.0880	$8140.297^{+0.027}_{-0.028}$	$0.172^{+0.002}_{-0.001}$	$42.19^{+0.21}_{-0.27}$	$-0.335^{+0.016}_{-0.019}$	$0.235^{+0.013}_{-0.010}$	$-0.14^{+0.03}_{-0.03}$	3565.9 / 3539	A
Gaia18akb	270.6288	-27.8430	$8178.376^{+0.025}_{-0.050}$	$0.516^{+0.035}_{-0.021}$	$48.97^{+1.74}_{-2.32}$	$0.779^{+0.023}_{-0.017}$	$0.175^{+0.023}_{-0.019}$	$1.37^{+0.44}_{-0.57}$	28280.2 / 4057	A
Gaia18bmt	214.0148	-56.9134	$8284.806^{+0.029}_{-0.030}$	$0.068^{+0.001}_{-0.001}$	$60.37^{+1.04}_{-0.83}$	$0.003^{+0.033}_{-0.036}$	$0.032^{+0.022}_{-0.019}$	$0.15^{+0.02}_{-0.02}$	1462.7 / 874	A
			$8284.803^{+0.033}_{-0.027}$	$-0.068^{+0.001}_{-0.002}$	$60.41^{+1.17}_{-0.95}$	$0.007^{+0.032}_{-0.043}$	$0.033^{+0.023}_{-0.019}$	$0.15^{+0.02}_{-0.02}$	1462.7 / 874	B
Gaia18ceb	264.8469	-35.2672	$8302.324^{+0.070}_{-0.059}$	$-0.909^{+0.032}_{-0.058}$	$49.82^{+1.33}_{-1.96}$	$0.394^{+0.138}_{-0.171}$	$0.260^{+0.026}_{-0.028}$	$-0.16^{+0.25}_{-0.28}$	717.5 / 736	A
Gaia18cer	263.9740	-27.5328	$8375.523^{+0.017}_{-0.016}$	$-0.434^{+0.005}_{-0.006}$	$43.85^{+0.43}_{-0.45}$	$0.004^{+0.034}_{-0.033}$	$0.458^{+0.010}_{-0.009}$	$-0.12^{+0.02}_{-0.02}$	204.0 / 643	A
			$8375.536^{+0.019}_{-0.015}$	$0.435^{+0.005}_{-0.005}$	$44.29^{+0.50}_{-0.41}$	$0.049^{+0.036}_{-0.026}$	$0.454^{+0.009}_{-0.009}$	$-0.12^{+0.02}_{-0.02}$	203.4 / 643	B
Gaia18ces	269.2658	-33.9361	$8450.954^{+0.415}_{-0.316}$	$0.898^{+0.115}_{-0.049}$	$32.54^{+0.96}_{-2.02}$	$-0.175^{+0.011}_{-0.022}$	$0.536^{+0.035}_{-0.015}$	$-0.83^{+0.06}_{-0.08}$	147774.0 / 1897	A
Gaia18cfc	268.5731	-30.5694	$8320.653^{+0.004}_{-0.004}$	$0.221^{+0.001}_{-0.001}$	$44.10^{+0.13}_{-0.11}$	$-0.079^{+0.064}_{-0.061}$	$0.267^{+0.018}_{-0.019}$	$-0.00^{+0.02}_{-0.02}$	931.3 / 2882	A
Gaia18cfs	268.6784	-22.8204	$8348.277^{+0.001}_{-0.001}$	$-0.022^{+0.001}_{-0.001}$	$40.98^{+0.18}_{-0.16}$	$-0.021^{+0.068}_{-0.070}$	$0.168^{+0.008}_{-0.008}$	$-0.12^{+0.01}_{-0.01}$	1355.5 / 731	A
Gaia18cgp	271.7968	-24.9823	$8315.840^{+0.001}_{-0.001}$	$-0.009^{+0.001}_{-0.001}$	$45.40^{+0.04}_{-0.04}$	$0.353^{+0.042}_{-0.052}$	$-0.063^{+0.006}_{-0.005}$	$0.16^{+0.01}_{-0.01}$	6037.7 / 743	A
Gaia18cib	279.1148	-16.5783	$8327.392^{+0.152}_{-0.085}$	$-0.004^{+0.022}_{-0.021}$	$77.18^{+5.52}_{-9.82}$	$-0.397^{+0.145}_{-0.423}$	$-0.250^{+0.102}_{-0.116}$	$0.06^{+0.10}_{-0.18}$	56.4 / 85	A
Gaia18cik	278.3799	-3.4032	$8364.093^{+2.302}_{-1.194}$	$0.212^{+0.067}_{-0.026}$	$211.34^{+16.62}_{-33.01}$	$0.103^{+0.022}_{-0.017}$	$-0.191^{+0.034}_{-0.067}$	$-0.20^{+0.13}_{-0.23}$	393.0 / 118	A
			$8362.627^{+1.043}_{-0.784}$	$-0.084^{+0.008}_{-0.028}$	$396.85^{+46.43}_{-96.29}$	$0.078^{+0.016}_{-0.022}$	$-0.061^{+0.008}_{-0.014}$	$1.30^{+0.26}_{-0.60}$	400.8 / 118	B
Gaia18cjk	283.7880	-6.6635	$8377.218^{+3.161}_{-8.601}$	$-0.156^{+0.020}_{-0.070}$	$214.16^{+23.81}_{-48.22}$	$-0.343^{+0.087}_{-0.144}$	$0.360^{+0.090}_{-0.037}$	$2.63^{+0.59}_{-1.20}$	1034.2 / 257	A
Gaia18clg	155.5824	-64.5504	$8378.023^{+0.699}_{-0.494}$	$0.104^{+0.034}_{-0.018}$	$150.98^{+25.29}_{-30.08}$	$0.270^{+0.056}_{-0.032}$	$0.116^{+0.041}_{-0.033}$	$0.07^{+0.24}_{-0.28}$	63.8 / 203	A
			$8378.425^{+0.583}_{-0.637}$	$-0.107^{+0.022}_{-0.027}$	$144.80^{+32.76}_{-23.62}$	$0.279^{+0.050}_{-0.036}$	$0.210^{+0.048}_{-0.052}$	$0.04^{+0.29}_{-0.22}$	63.7 / 203	B
Gaia18cmk	307.1494	22.8305	$8362.444^{+0.064}_{-0.075}$	$0.386^{+0.020}_{-0.021}$	$31.15^{+1.35}_{-1.00}$	$-0.504^{+0.147}_{-0.075}$	$-0.596^{+0.112}_{-0.059}$	$0.21^{+0.10}_{-0.08}$	5617.5 / 894	A
Gaia18cnm	275.8788	-7.3327	$8391.009^{+0.498}_{-1.233}$	$0.611^{+0.133}_{-0.185}$	$54.94^{+33.32}_{-6.61}$	$-0.073^{+0.495}_{-0.110}$	$-0.299^{+0.014}_{-0.106}$	$-0.29^{+0.53}_{-0.20}$	2691.1 / 898	A
Gaia18cov	108.6160	-20.9863	$8422.671^{+1.218}_{-2.474}$	$-0.314^{+0.044}_{-0.160}$	$120.24^{+20.57}_{-38.71}$	$0.032^{+0.043}_{-0.124}$	$-0.307^{+0.020}_{-0.043}$	$1.13^{+0.47}_{-0.95}$	1683.7 / 616	A
Gaia18cwh	264.4138	-35.3457	$8417.155^{+0.090}_{-0.195}$	$-0.001^{+0.009}_{-0.006}$	$84.64^{+7.23}_{-4.92}$	$0.049^{+0.097}_{-0.099}$	$-0.082^{+0.036}_{-0.033}$	$0.93^{+0.67}_{-0.38}$	585.6 / 706	A
Gaia18dep	135.1505	-56.5469	$8419.245^{+0.723}_{-0.888}$	$-0.160^{+0.022}_{-0.026}$	$101.80^{+13.08}_{-11.74}$	$-0.027^{+0.035}_{-0.037}$	$-0.625^{+0.062}_{-0.060}$	$5.02^{+1.05}_{-0.99}$	644.8 / 966	A
Gaia18dif	197.5516	-58.8041	$8525.322^{+0.066}_{-0.088}$	$-0.176^{+0.007}_{-0.009}$	$215.09^{+9.52}_{-9.75}$	$-0.086^{+0.006}_{-0.007}$	$-0.052^{+0.004}_{-0.005}$	$0.98^{+0.11}_{-0.11}$	1681.6 / 740	A
			$8524.862^{+0.137}_{-0.144}$	$0.266^{+0.015}_{-0.013}$	$198.06^{+7.26}_{-7.40}$	$-0.079^{+0.005}_{-0.005}$	$-0.035^{+0.003}_{-0.003}$	$0.19^{+0.08}_{-0.08}$	1637.0 / 740	B
Gaia18dma	295.3575	13.8726	$8445.942^{+0.169}_{-0.157}$	$-0.079^{+0.007}_{-0.009}$	$107.60^{+9.36}_{-9.74}$	$0.278^{+0.055}_{-0.053}$	$-0.757^{+0.038}_{-0.043}$	$0.52^{+0.17}_{-0.17}$	7648.2 / 237	A
			$8445.085^{+0.249}_{-0.315}$	$0.080^{+0.008}_{-0.009}$	$125.29^{+15.59}_{-11.69}$	$0.215^{+0.058}_{-0.059}$	$-0.849^{+0.045}_{-0.047}$	$0.48^{+0.19}_{-0.15}$	7651.7 / 237	B
Gaia18dml	292.1442	23.1339	$8495.592^{+1.181}_{-0.692}$	$0.166^{+0.561}_{-0.201}$	$95.74^{+31.79}_{-48.81}$	$0.084^{+0.087}_{-0.021}$	$0.209^{+0.309}_{-0.074}$	$3.95^{+2.80}_{-3.94}$	2655.2 / 1281	A
Gaia18eaz	219.3758	-67.2788	$8497.233^{+2.745}_{-0.594}$	$-0.075^{+0.067}_{-0.003}$	$39.32^{+3.53}_{-4.45}$	$-0.386^{+0.399}_{-0.169}$	$-0.194^{+0.043}_{-0.178}$	$-0.17^{+0.13}_{-0.25}$	100.3 / 297	A

Notes. Microlensing model parameters are reported as $x^{+\sigma_+}_{-\sigma_-}$, with uncertainties corresponding to the 16th and 84th percentiles.

Table A.3. Model parameters for GSA alerts from 2019.

Event	RA (°)	Dec (°)	t_0 (HJD')	u_0	t_E (days)	$\pi_{E,N}$	$\pi_{E,E}$	f_b/f_s	χ^2 / dof	Mod.
Gaia19aqf	287.9695	3.9495	$8545.968^{+1.408}_{-0.470}$	$-0.113^{+0.011}_{-0.150}$	$209.69^{+18.27}_{-101.05}$	$-0.258^{+0.036}_{-0.018}$	$0.080^{+0.017}_{-0.018}$	$3.03^{+0.47}_{-2.57}$	795.4 / 656	A
			$8545.042^{+1.357}_{-1.362}$	$0.332^{+0.361}_{-0.056}$	$110.73^{+13.25}_{-44.71}$	$-0.319^{+0.059}_{-0.035}$	$0.277^{+0.103}_{-0.039}$	$0.07^{+0.23}_{-0.71}$	794.2 / 656	B
Gaia19aqw	182.2558	-68.0368	$8516.198^{+0.047}_{-0.046}$	$-0.060^{+0.002}_{-0.002}$	$81.46^{+1.20}_{-1.31}$	$-0.276^{+0.007}_{-0.008}$	$-0.257^{+0.006}_{-0.008}$	$-0.04^{+0.02}_{-0.02}$	313.2 / 704	A
Gaia19asx	289.1144	26.6535	$8566.298^{+0.044}_{-0.054}$	$0.109^{+0.003}_{-0.004}$	$40.09^{+0.99}_{-0.77}$	$0.953^{+0.023}_{-0.036}$	$0.283^{+0.015}_{-0.019}$	$0.62^{+0.06}_{-0.05}$	5221.2 / 1168	A
			$8566.295^{+0.055}_{-0.057}$	$-0.107^{+0.003}_{-0.004}$	$42.58^{+0.95}_{-1.00}$	$0.878^{+0.029}_{-0.029}$	$0.260^{+0.016}_{-0.017}$	$0.65^{+0.06}_{-0.06}$	5223.9 / 1168	B
Gaia19awc	273.9006	-2.2570	$8612.638^{+0.136}_{-0.118}$	$0.314^{+0.021}_{-0.021}$	$64.62^{+4.56}_{-3.89}$	$-0.038^{+0.116}_{-0.119}$	$-0.075^{+0.025}_{-0.027}$	$0.00^{+0.10}_{-0.09}$	3949.5 / 1107	A
Gaia19ayo	265.2167	-36.0396	$8534.788^{+0.015}_{-0.007}$	$0.062^{+0.002}_{-0.002}$	$57.66^{+1.36}_{-1.95}$	$-0.385^{+0.539}_{-0.012}$	$0.323^{+0.008}_{-0.074}$	$0.25^{+0.04}_{-0.03}$	169.5 / 617	A
			$8534.791^{+0.012}_{-0.008}$	$-0.063^{+0.002}_{-0.001}$	$56.40^{+1.76}_{-1.08}$	$0.155^{+0.015}_{-0.550}$	$0.284^{+0.042}_{-0.029}$	$0.23^{+0.05}_{-0.02}$	169.5 / 617	B
Gaia19bcm	156.8948	-71.7010	$8551.198^{+0.030}_{-0.038}$	$-0.271^{+0.011}_{-0.011}$	$31.93^{+1.16}_{-1.04}$	$-0.174^{+0.034}_{-0.035}$	$0.498^{+0.129}_{-0.134}$	$0.07^{+0.06}_{-0.05}$	2300.8 / 1380	A
Gaia19bht	268.8967	-29.0048	$8574.830^{+0.012}_{-0.015}$	$-0.319^{+0.003}_{-0.003}$	$54.98^{+0.51}_{-0.42}$	$-0.042^{+0.048}_{-0.043}$	$-0.267^{+0.004}_{-0.003}$	$1.60^{+0.10}_{-0.09}$	4128.3 / 709	A
Gaia19bhw	267.3231	-30.8515	$8589.946^{+0.280}_{-0.372}$	$0.301^{+0.050}_{-0.034}$	$78.09^{+7.91}_{-8.85}$	$-0.428^{+0.085}_{-0.080}$	$0.042^{+0.031}_{-0.022}$	$1.45^{+1.63}_{-1.11}$	127.5 / 381	A
Gaia19bii	269.5016	-33.7132	$8554.110^{+0.001}_{-0.002}$	$0.062^{+0.001}_{-0.001}$	$34.16^{+0.04}_{-0.04}$	$0.298^{+0.019}_{-0.019}$	$0.004^{+0.002}_{-0.003}$	$0.03^{+0.01}_{-0.01}$	6381.9 / 1234	A
Gaia19bir	234.6434	-51.2415	$8612.348^{+9.933}_{-2.458}$	$-0.066^{+0.205}_{-0.269}$	$128.82^{+14.81}_{-76.79}$	$0.011^{+0.107}_{-0.021}$	$-0.289^{+0.040}_{-0.444}$	$0.29^{+0.15}_{-1.10}$	8.6 / 41	A
Gaia19bjq	55.1976	57.9558	$8618.113^{+0.220}_{-0.228}$	$-0.121^{+0.014}_{-0.013}$	$132.69^{+3.40}_{-3.62}$	$-0.214^{+0.003}_{-0.005}$	$0.217^{+0.007}_{-0.004}$	$0.06^{+0.05}_{-0.05}$	2202.2 / 1449	A
Gaia19brt	297.7061	34.6373	$8650.944^{+0.007}_{-0.006}$	$0.015^{+0.001}_{-0.001}$	$103.66^{+2.45}_{-2.24}$	$-0.046^{+0.011}_{-0.015}$	$-0.103^{+0.019}_{-0.014}$	$6.94^{+0.23}_{-0.21}$	7124.0 / 1555	A
Gaia19chi	232.0353	-67.0209	$8637.369^{+1.496}_{-1.235}$	$0.221^{+0.116}_{-0.082}$	$133.68^{+63.71}_{-37.22}$	$0.110^{+0.040}_{-0.029}$	$0.185^{+0.020}_{-0.047}$	$1.60^{+1.97}_{-1.11}$	362.3 / 240	A
			$8637.061^{+2.727}_{-1.176}$	$-0.330^{+0.156}_{-0.154}$	$101.00^{+83.75}_{-27.55}$	$0.302^{+0.067}_{-0.074}$	$0.131^{+0.063}_{-0.077}$	$0.54^{+1.95}_{-0.66}$	361.8 / 240	B
Gaia19cyv	318.2633	43.3376	$8728.572^{+0.037}_{-0.036}$	$0.453^{+0.018}_{-0.015}$	$48.33^{+1.23}_{-1.37}$	$-0.566^{+0.018}_{-0.021}$	$-0.418^{+0.018}_{-0.019}$	$-0.13^{+0.04}_{-0.05}$	6036.4 / 1116	A
			$8728.913^{+0.054}_{-0.053}$	$-0.461^{+0.017}_{-0.018}$	$56.20^{+1.37}_{-1.37}$	$-0.474^{+0.016}_{-0.016}$	$-0.268^{+0.009}_{-0.009}$	$-0.16^{+0.05}_{-0.05}$	5934.7 / 1116	B
Gaia19dae	309.0341	32.7209	$8720.933^{+0.306}_{-0.172}$	$0.467^{+0.069}_{-0.040}$	$119.20^{+11.42}_{-14.89}$	$0.204^{+0.011}_{-0.021}$	$0.119^{+0.014}_{-0.021}$	$0.70^{+0.24}_{-0.32}$	14915.3 / 2548	A
			$8721.314^{+0.108}_{-0.127}$	$-0.404^{+0.028}_{-0.037}$	$107.34^{+5.82}_{-6.48}$	$0.108^{+0.004}_{-0.006}$	$0.115^{+0.007}_{-0.010}$	$1.10^{+0.23}_{-0.25}$	14890.7 / 2548	B
Gaia19dak	302.3652	29.9359	$8898.094^{+0.892}_{-1.078}$	$0.397^{+0.009}_{-0.007}$	$216.24^{+3.17}_{-3.47}$	$-0.199^{+0.004}_{-0.005}$	$0.436^{+0.007}_{-0.005}$	$-0.08^{+0.02}_{-0.02}$	10803.1 / 1524	A
			$8949.083^{+1.031}_{-0.813}$	$0.011^{+0.004}_{-0.002}$	$268.92^{+3.64}_{-3.71}$	$-0.043^{+0.003}_{-0.003}$	$0.401^{+0.006}_{-0.006}$	$0.02^{+0.02}_{-0.02}$	10822.8 / 1524	B
Gaia19drc	262.8726	-30.3847	$8720.391^{+0.078}_{-0.077}$	$0.329^{+0.025}_{-0.023}$	$80.35^{+4.46}_{-4.13}$	$-0.425^{+0.027}_{-0.021}$	$0.170^{+0.015}_{-0.014}$	$1.70^{+0.95}_{-0.70}$	976.1 / 630	A
Gaia19dtd	272.9919	-29.9231	$8693.259^{+0.046}_{-0.044}$	$-0.613^{+0.011}_{-0.014}$	$63.80^{+0.56}_{-0.67}$	$-0.150^{+0.033}_{-0.038}$	$0.010^{+0.009}_{-0.010}$	$-0.01^{+0.03}_{-0.04}$	3487.7 / 2782	A
			$8693.284^{+0.046}_{-0.041}$	$0.653^{+0.021}_{-0.017}$	$60.27^{+0.97}_{-1.10}$	$0.094^{+0.019}_{-0.018}$	$-0.012^{+0.012}_{-0.011}$	$-0.11^{+0.04}_{-0.05}$	3488.7 / 2782	B
Gaia19dtk	280.4294	-28.4836	$8829.584^{+5.523}_{-6.444}$	$-0.217^{+0.043}_{-0.075}$	$162.62^{+49.89}_{-44.22}$	$0.427^{+0.134}_{-0.088}$	$0.292^{+0.148}_{-0.100}$	$0.63^{+4.20}_{-1.30}$	32.0 / 70	A
			$8847.487^{+5.514}_{-6.421}$	$0.049^{+0.040}_{-0.041}$	$232.25^{+104.18}_{-56.90}$	$-0.274^{+0.056}_{-0.068}$	$0.325^{+0.134}_{-0.120}$	$1.23^{+9.43}_{-1.84}$	34.0 / 70	B
Gaia19dur	283.8717	-10.7520	$8690.619^{+0.012}_{-0.010}$	$-0.012^{+0.001}_{-0.001}$	$130.78^{+4.66}_{-5.30}$	$0.128^{+0.015}_{-0.020}$	$-0.211^{+0.019}_{-0.018}$	$-0.35^{+0.03}_{-0.03}$	221.0 / 179	A
Gaia19duw	298.1994	42.0715	$8752.670^{+1.418}_{-0.606}$	$0.148^{+0.079}_{-0.026}$	$97.44^{+9.00}_{-18.89}$	$-0.396^{+0.034}_{-0.097}$	$-0.034^{+0.006}_{-0.016}$	$0.69^{+0.29}_{-0.57}$	49.9 / 139	A
Gaia19eca	272.2020	-24.8825	$8719.303^{+0.003}_{-0.003}$	$0.057^{+0.001}_{-0.001}$	$83.43^{+0.14}_{-0.15}$	$0.143^{+0.008}_{-0.009}$	$0.286^{+0.001}_{-0.001}$	$-0.07^{+0.01}_{-0.01}$	7865.1 / 1352	A
Gaia19ect	269.3059	-29.4579	$8755.940^{+0.006}_{-0.006}$	$0.129^{+0.001}_{-0.001}$	$84.24^{+0.59}_{-0.67}$	$0.385^{+0.009}_{-0.010}$	$-0.040^{+0.002}_{-0.002}$	$-0.15^{+0.02}_{-0.02}$	13132.6 / 1323	A
Gaia19eim	200.7762	-63.4019	$8802.284^{+0.257}_{-0.306}$	$-0.132^{+0.327}_{-0.265}$	$63.53^{+8.07}_{-20.86}$	$-0.040^{+0.047}_{-0.109}$	$0.287^{+0.200}_{-0.069}$	$0.05^{+0.23}_{-0.65}$	149.1 / 160	A
Gaia19eku	165.2140	-61.7568	$8796.102^{+2.704}_{-3.405}$	$-0.211^{+0.393}_{-0.498}$	$183.02^{+274.51}_{-125.43}$	$0.003^{+0.077}_{-0.227}$	$-0.158^{+0.081}_{-0.038}$	$0.40^{+1.57}_{-1.23}$	51.4 / 113	A
Gaia19enj	303.0627	34.9701	$8749.048^{+2.618}_{-0.195}$	$-0.040^{+0.092}_{-0.256}$	$73.63^{+5.90}_{-20.48}$	$-0.370^{+0.056}_{-0.177}$	$-0.181^{+0.034}_{-0.073}$	$0.05^{+0.12}_{-0.60}$	401.8 / 257	A
Gaia19esp	194.2462	-63.8131	$8870.517^{+0.191}_{-0.171}$	$-0.125^{+0.015}_{-0.012}$	$98.85^{+12.65}_{-7.60}$	$0.152^{+0.047}_{-0.035}$	$-0.104^{+0.026}_{-0.021}$	$0.67^{+0.26}_{-0.16}$	1085.0 / 404	A
Gaia19evd	158.1360	-63.2424	$8810.835^{+0.836}_{-0.619}$	$-0.279^{+0.424}_{-0.223}$	$96.10^{+133.71}_{-33.17}$	$-0.078^{+0.145}_{-0.139}$	$-0.189^{+0.082}_{-0.067}$	$0.92^{+4.07}_{-1.10}$	81.3 / 150	A
Gaia19fnb	197.7973	-65.3135	$8857.737^{+1.545}_{-1.345}$	$0.136^{+0.060}_{-0.037}$	$108.97^{+28.02}_{-24.93}$	$-0.196^{+0.076}_{-0.098}$	$-0.198^{+0.043}_{-0.066}$	$2.03^{+1.21}_{-1.04}$	142.7 / 172	A

Notes. Microlensing model parameters are reported as $x^{+\sigma_+}_{-\sigma_-}$, with uncertainties corresponding to the 16th and 84th percentiles.

Appendix B: Lens parameters

Table B.1. Lens mass and distance parameters for GSA alerts from 2017.

Name	Model	M_L [$M_\odot$]				D_L [kpc]			
		pyL+D_S	pyL	BGM+D_S	BGM	pyL+D_S	pyL	BGM+D_S	BGM
Gaia17aqu	A	$0.46^{+0.08}_{-0.07}$	$0.60^{+0.10}_{-0.08}$	$0.42^{+0.34}_{-0.21}$	$0.45^{+0.33}_{-0.21}$	$2.84^{+0.69}_{-0.47}$	$4.58^{+1.87}_{-0.97}$	$2.84^{+0.82}_{-0.70}$	$3.66^{+1.59}_{-1.13}$
Gaia17bbs	A	$0.46^{+0.12}_{-0.10}$	$0.50^{+0.12}_{-0.09}$	$0.82^{+0.21}_{-0.16}$	$0.77^{+0.30}_{-0.25}$	$5.54^{+1.31}_{-1.06}$	$6.13^{+1.45}_{-1.19}$	$3.40^{+0.92}_{-0.70}$	$2.74^{+0.73}_{-0.63}$
Gaia17bdk	A	$0.33^{+0.08}_{-0.07}$	$0.20^{+0.10}_{-0.06}$	$0.98^{+0.29}_{-0.17}$	$0.99^{+0.24}_{-0.21}$	$9.41^{+1.02}_{-0.68}$	$5.76^{+0.67}_{-0.47}$	$5.93^{+1.26}_{-1.29}$	$6.77^{+2.02}_{-1.62}$
Gaia17bej	A	$0.61^{+0.08}_{-0.06}$	$0.62^{+0.10}_{-0.08}$	$0.50^{+0.28}_{-0.20}$	$0.50^{+0.28}_{-0.19}$	$3.39^{+0.64}_{-0.62}$	$3.96^{+0.87}_{-0.61}$	$3.60^{+1.12}_{-1.05}$	$3.44^{+1.50}_{-1.26}$
Gaia17cah	A	$0.10^{+0.01}_{-0.01}$	$0.10^{+0.02}_{-0.01}$	$0.10^{+0.04}_{-0.03}$	$0.12^{+0.04}_{-0.04}$	$4.42^{+0.41}_{-0.33}$	$5.57^{+0.47}_{-0.58}$	$4.28^{+0.47}_{-0.48}$	$4.38^{+1.09}_{-0.97}$

Notes. Parameters are reported as $x^{+\sigma_+}_{-\sigma_-}$, with uncertainties corresponding to the 16th and 84th percentiles.

Table B.2. Lens mass and distance parameters for GSA alerts from 2018.

Name	Model	M_L [$M_\odot$]				D_L [kpc]			
		pyL+D_S	pyL	BGM+D_S	BGM	pyL+D_S	pyL	BGM+D_S	BGM
Gaia18ajt	A	$0.11^{+0.02}_{-0.01}$	$0.10^{+0.01}_{-0.01}$	$0.12^{+0.13}_{-0.03}$	$0.23^{+0.05}_{-0.04}$	$4.27^{+0.41}_{-0.47}$	$3.92^{+0.35}_{-0.28}$	$3.67^{+0.92}_{-1.20}$	$2.46^{+0.74}_{-0.36}$
Gaia18akb	A	$0.35^{+0.03}_{-0.02}$	$0.17^{+0.01}_{-0.01}$	$0.11^{+0.14}_{-0.01}$	$0.11^{+0.01}_{-0.01}$	$0.51^{+0.03}_{-0.04}$	$1.09^{+0.06}_{-0.03}$	$1.28^{+0.08}_{-0.61}$	$1.32^{+0.07}_{-0.06}$
Gaia18bmt	A	$1.27^{+0.24}_{-0.18}$	$0.85^{+0.16}_{-0.10}$	$0.89^{+0.32}_{-0.36}$	$0.77^{+0.33}_{-0.26}$	$6.02^{+0.44}_{-0.48}$	$2.78^{+0.41}_{-0.29}$	$4.53^{+0.53}_{-0.48}$	$5.03^{+1.67}_{-2.18}$
	B	$1.21^{+0.21}_{-0.23}$	$1.43^{+0.21}_{-0.16}$	$0.82^{+0.40}_{-0.79}$	$0.85^{+0.43}_{-0.34}$	$6.78^{+0.76}_{-0.70}$	$8.61^{+2.09}_{-1.65}$	$4.45^{+1.03}_{-0.48}$	$5.06^{+1.55}_{-1.74}$
Gaia18ceb	A	$0.10^{+0.01}_{-0.01}$	$0.10^{+0.01}_{-0.01}$	$0.74^{+0.43}_{-0.11}$	$0.74^{+0.24}_{-0.22}$	$4.50^{+0.60}_{-0.63}$	$5.66^{+0.68}_{-0.57}$	$2.94^{+1.49}_{-0.58}$	$2.88^{+1.64}_{-1.57}$
Gaia18cer	A	$0.09^{+0.01}_{-0.01}$	$0.09^{+0.01}_{-0.01}$	$0.07^{+0.01}_{-0.01}$	$0.11^{+0.01}_{-0.02}$	$3.21^{+0.25}_{-0.24}$	$4.35^{+0.30}_{-0.36}$	$3.16^{+0.19}_{-0.24}$	$3.39^{+0.31}_{-0.24}$
	B	$0.10^{+0.01}_{-0.01}$	$0.09^{+0.01}_{-0.01}$	$0.25^{+0.06}_{-0.17}$	$0.12^{+0.02}_{-0.08}$	$3.66^{+0.28}_{-0.24}$	$4.24^{+0.27}_{-0.28}$	$1.69^{+1.29}_{-0.20}$	$3.27^{+0.74}_{-0.33}$
Gaia18ces	A	$0.09^{+0.01}_{-0.01}$	$0.09^{+0.01}_{-0.01}$	$0.20^{+0.02}_{-0.03}$	$0.19^{+0.03}_{-0.08}$	$2.28^{+0.19}_{-0.21}$	$1.86^{+0.13}_{-0.11}$	$1.45^{+0.15}_{-0.10}$	$1.47^{+1.17}_{-0.11}$
Gaia18cfc	A	$0.12^{+0.03}_{-0.03}$	$0.13^{+0.03}_{-0.02}$	$0.18^{+0.14}_{-0.06}$	$0.16^{+0.15}_{-0.05}$	$5.54^{+0.72}_{-0.65}$	$6.32^{+0.78}_{-0.71}$	$5.36^{+1.14}_{-1.68}$	$3.97^{+1.39}_{-0.84}$
Gaia18cfs	A	$0.10^{+0.01}_{-0.01}$	$0.10^{+0.01}_{-0.01}$	$0.77^{+0.16}_{-0.13}$	$0.71^{+0.15}_{-0.12}$	$9.63^{+0.82}_{-0.72}$	$10.36^{+0.61}_{-0.86}$	$3.32^{+0.84}_{-0.57}$	$3.32^{+0.71}_{-0.51}$
Gaia18cgp	A	$0.63^{+0.09}_{-0.06}$	$0.47^{+0.06}_{-0.07}$	$0.46^{+0.10}_{-0.08}$	$0.41^{+0.40}_{-0.09}$	$5.55^{+0.59}_{-0.59}$	$2.40^{+0.35}_{-0.26}$	$1.07^{+0.12}_{-0.13}$	$1.62^{+2.48}_{-0.74}$
Gaia18cib	A	$0.27^{+0.12}_{-0.08}$	$0.33^{+0.11}_{-0.09}$	$0.33^{+0.31}_{-0.17}$	$0.37^{+0.35}_{-0.23}$	$2.34^{+1.08}_{-0.72}$	$3.53^{+2.36}_{-1.41}$	$3.45^{+1.37}_{-1.37}$	$3.84^{+2.56}_{-1.73}$
Gaia18cik	A	$0.13^{+0.05}_{-0.03}$	$0.14^{+0.05}_{-0.03}$	$0.87^{+0.25}_{-0.20}$	$0.81^{+0.28}_{-0.21}$	$7.04^{+1.36}_{-1.18}$	$7.37^{+1.46}_{-1.44}$	$2.75^{+1.21}_{-0.76}$	$2.16^{+1.05}_{-0.61}$
	B	$0.69^{+0.11}_{-0.11}$	$0.69^{+0.12}_{-0.09}$	$1.00^{+0.24}_{-0.17}$	$1.01^{+0.29}_{-0.19}$	$7.17^{+1.40}_{-1.44}$	$7.41^{+1.39}_{-1.25}$	$5.33^{+1.34}_{-1.03}$	$4.65^{+1.64}_{-1.53}$
Gaia18cjk	A	$0.83^{+0.10}_{-0.10}$	$0.72^{+0.06}_{-0.05}$	$0.29^{+0.26}_{-0.19}$	$0.31^{+0.34}_{-0.18}$	$3.32^{+0.38}_{-0.46}$	$4.61^{+0.98}_{-0.62}$	$1.84^{+0.65}_{-0.75}$	$2.83^{+1.81}_{-1.15}$
Gaia18clg	A	$0.26^{+0.06}_{-0.05}$	$0.29^{+0.05}_{-0.07}$	$0.40^{+0.37}_{-0.20}$	$0.37^{+0.31}_{-0.18}$	$2.27^{+0.30}_{-0.26}$	$3.30^{+0.86}_{-0.60}$	$1.82^{+0.61}_{-0.57}$	$2.62^{+1.27}_{-0.99}$
	B	$0.21^{+0.07}_{-0.07}$	$0.25^{+0.07}_{-0.05}$	$0.32^{+0.34}_{-0.15}$	$0.31^{+0.30}_{-0.14}$	$2.25^{+0.38}_{-0.35}$	$3.27^{+0.88}_{-0.60}$	$1.70^{+0.57}_{-0.57}$	$2.39^{+1.16}_{-0.95}$
Gaia18cmk	A	$0.21^{+0.04}_{-0.04}$	$0.25^{+0.06}_{-0.05}$	$0.13^{+0.09}_{-0.06}$	$0.12^{+0.11}_{-0.06}$	$0.83^{+0.13}_{-0.12}$	$1.01^{+0.24}_{-0.15}$	$1.27^{+0.49}_{-0.38}$	$1.61^{+1.13}_{-0.65}$
Gaia18cnm	A	$0.10^{+0.01}_{-0.01}$	$0.09^{+0.01}_{-0.01}$	$0.45^{+0.21}_{-0.10}$	$0.46^{+0.26}_{-0.11}$	$7.53^{+1.24}_{-1.06}$	$4.93^{+0.82}_{-0.60}$	$1.45^{+0.88}_{-0.40}$	$1.45^{+0.83}_{-0.45}$
Gaia18cov	A	$0.53^{+0.07}_{-0.06}$	$0.83^{+0.08}_{-0.08}$	$0.33^{+0.28}_{-0.15}$	$0.32^{+0.27}_{-0.15}$	$1.72^{+0.29}_{-0.21}$	$5.32^{+0.68}_{-0.92}$	$1.80^{+0.53}_{-0.50}$	$2.39^{+1.23}_{-0.82}$
Gaia18cwh	A	$0.69^{+0.07}_{-0.09}$	$0.79^{+0.11}_{-0.11}$	$0.91^{+0.21}_{-0.16}$	$0.90^{+0.21}_{-0.17}$	$6.85^{+1.02}_{-1.70}$	$8.50^{+1.59}_{-1.48}$	$5.15^{+2.12}_{-1.45}$	$5.14^{+2.34}_{-1.59}$
Gaia18dep	A	$1.53^{+0.12}_{-0.41}$	$0.53^{+0.07}_{-0.04}$	$0.18^{+0.51}_{-0.06}$	$0.18^{+0.19}_{-0.09}$	$3.90^{+0.04}_{-0.03}$	$0.70^{+0.09}_{-0.09}$	$1.09^{+0.24}_{-0.70}$	$1.37^{+1.04}_{-0.55}$
Gaia18dif	A	$0.76^{+0.09}_{-0.10}$	$0.87^{+0.12}_{-0.12}$	$0.98^{+0.43}_{-0.39}$	$0.87^{+0.48}_{-0.35}$	$3.89^{+0.32}_{-0.25}$	$6.79^{+0.67}_{-0.76}$	$3.11^{+0.53}_{-0.41}$	$4.44^{+1.39}_{-1.21}$
	B	$0.67^{+0.10}_{-0.10}$	$0.79^{+0.08}_{-0.11}$	$1.01^{+0.49}_{-0.49}$	$0.79^{+0.49}_{-0.34}$	$4.12^{+0.45}_{-0.33}$	$7.61^{+0.69}_{-0.68}$	$3.44^{+0.56}_{-0.48}$	$4.55^{+1.74}_{-1.16}$
Gaia18dma	A	$0.18^{+0.06}_{-0.03}$	$0.14^{+0.01}_{-0.01}$	$0.08^{+0.07}_{-0.04}$	$0.09^{+0.09}_{-0.05}$	$0.96^{+0.12}_{-0.22}$	$1.25^{+0.14}_{-0.13}$	$1.81^{+1.09}_{-0.69}$	$1.60^{+1.10}_{-0.67}$
	B	$0.15^{+0.02}_{-0.01}$	$0.17^{+0.03}_{-0.02}$	$0.06^{+0.06}_{-0.03}$	$0.07^{+0.10}_{-0.03}$	$1.01^{+0.13}_{-0.11}$	$0.88^{+0.17}_{-0.12}$	$1.97^{+0.88}_{-0.76}$	$1.92^{+0.92}_{-0.84}$
Gaia18dml	A	$0.80^{+0.18}_{-0.12}$	$0.91^{+0.13}_{-0.16}$	$0.43^{+0.43}_{-0.25}$	$0.47^{+0.41}_{-0.26}$	$4.84^{+0.85}_{-0.65}$	$6.34^{+1.25}_{-1.02}$	$2.66^{+0.96}_{-0.82}$	$4.86^{+2.61}_{-1.88}$
Gaia18eaz	A	$0.09^{+0.01}_{-0.01}$	$0.10^{+0.02}_{-0.01}$	$0.23^{+0.21}_{-0.10}$	$0.22^{+0.22}_{-0.11}$	$3.15^{+0.40}_{-0.42}$	$8.05^{+1.85}_{-1.57}$	$2.27^{+0.77}_{-0.67}$	$2.93^{+1.58}_{-1.08}$

Notes. Parameters are reported as $x^{+\sigma_+}_{-\sigma_-}$, with uncertainties corresponding to the 16th and 84th percentiles.

Table B.3. Lens mass and distance parameters for GSA alerts from 2019.

Name	Model	M_L [$M_\odot$]				D_L [kpc]			
		pyL+D_S	pyL	BGM+D_S	BGM	pyL+D_S	pyL	BGM+D_S	BGM
Gaia19aqf	A	$0.59^{+0.06}_{-0.06}$	$0.56^{+0.12}_{-0.06}$	$0.35^{+0.38}_{-0.17}$	$0.28^{+0.28}_{-0.14}$	$2.43^{+0.38}_{-0.30}$	$2.44^{+0.54}_{-0.33}$	$2.56^{+0.89}_{-0.91}$	$3.32^{+1.87}_{-1.32}$
	B	$0.22^{+0.05}_{-0.05}$	$0.28^{+0.07}_{-0.06}$	$0.25^{+0.25}_{-0.13}$	$0.23^{+0.23}_{-0.13}$	$2.23^{+0.43}_{-0.34}$	$2.18^{+0.65}_{-0.48}$	$2.28^{+0.82}_{-1.03}$	$2.70^{+1.89}_{-1.07}$
Gaia19aqw	A	$0.11^{+0.02}_{-0.02}$	$0.11^{+0.02}_{-0.01}$	$0.24^{+0.24}_{-0.09}$	$0.31^{+0.26}_{-0.14}$	$4.58^{+0.54}_{-0.46}$	$4.63^{+0.48}_{-0.50}$	$2.38^{+1.02}_{-0.75}$	$1.69^{+1.17}_{-0.62}$
Gaia19asx	A	$0.15^{+0.01}_{-0.01}$	$0.19^{+0.01}_{-0.01}$	$0.06^{+0.07}_{-0.03}$	$0.06^{+0.05}_{-0.04}$	$0.74^{+0.05}_{-0.05}$	$0.59^{+0.04}_{-0.02}$	$1.35^{+0.66}_{-0.55}$	$1.40^{+1.46}_{-0.49}$
	B	$0.25^{+0.02}_{-0.03}$	$0.16^{+0.02}_{-0.02}$	$0.07^{+0.08}_{-0.04}$	$0.07^{+0.06}_{-0.03}$	$0.55^{+0.08}_{-0.05}$	$0.82^{+0.12}_{-0.08}$	$1.49^{+0.85}_{-0.65}$	$1.44^{+0.83}_{-0.55}$
Gaia19awc	A	$0.21^{+0.09}_{-0.06}$	$0.34^{+0.07}_{-0.10}$	$0.75^{+0.22}_{-0.21}$	$0.64^{+0.28}_{-0.25}$	$4.90^{+0.62}_{-0.76}$	$9.72^{+1.07}_{-1.32}$	$3.54^{+0.62}_{-0.46}$	$3.40^{+3.13}_{-1.62}$
Gaia19ayo	A	$0.33^{+0.06}_{-0.05}$	$0.74^{+0.05}_{-0.05}$	$0.29^{+0.39}_{-0.15}$	$0.29^{+0.28}_{-0.13}$	$3.23^{+0.45}_{-0.45}$	$6.92^{+0.97}_{-0.59}$	$4.38^{+1.71}_{-1.05}$	$4.18^{+2.29}_{-1.21}$
	B	$0.40^{+0.05}_{-0.07}$	$0.38^{+0.07}_{-0.06}$	$0.23^{+0.30}_{-0.12}$	$0.24^{+0.29}_{-0.15}$	$2.92^{+0.60}_{-0.55}$	$3.18^{+0.59}_{-0.71}$	$4.16^{+1.72}_{-1.12}$	$4.38^{+3.01}_{-1.24}$
Gaia19bcm	A	$0.64^{+0.13}_{-0.10}$	$0.60^{+0.11}_{-0.10}$	$0.16^{+0.12}_{-0.05}$	$0.24^{+0.29}_{-0.12}$	$1.26^{+0.63}_{-0.30}$	$1.28^{+0.30}_{-0.30}$	$2.04^{+0.70}_{-0.50}$	$1.39^{+0.92}_{-0.63}$
Gaia19bht	A	$0.59^{+0.06}_{-0.06}$	$0.58^{+0.05}_{-0.06}$	$0.17^{+0.30}_{-0.06}$	$0.18^{+0.30}_{-0.06}$	$1.96^{+0.15}_{-0.16}$	$2.38^{+0.16}_{-0.20}$	$4.72^{+0.51}_{-2.16}$	$4.68^{+0.65}_{-2.13}$
Gaia19bhw	A	$0.80^{+0.11}_{-0.12}$	$0.62^{+0.14}_{-0.10}$	$0.39^{+0.17}_{-0.14}$	$0.38^{+0.20}_{-0.19}$	$7.41^{+0.76}_{-1.13}$	$5.27^{+1.99}_{-1.51}$	$3.69^{+1.70}_{-1.02}$	$3.67^{+2.95}_{-1.05}$
Gaia19bii	A	$0.58^{+0.08}_{-0.06}$	$0.56^{+0.06}_{-0.05}$	$0.10^{+0.09}_{-0.03}$	$0.23^{+0.09}_{-0.09}$	$1.97^{+0.15}_{-0.21}$	$2.02^{+0.23}_{-0.15}$	$5.18^{+0.85}_{-1.22}$	$3.21^{+0.92}_{-0.61}$
Gaia19bir	A	$0.41^{+0.15}_{-0.12}$	$0.49^{+0.14}_{-0.16}$	$0.36^{+0.39}_{-0.21}$	$0.39^{+0.37}_{-0.22}$	$3.89^{+2.46}_{-1.47}$	$5.94^{+3.05}_{-2.59}$	$3.65^{+1.65}_{-1.25}$	$4.12^{+2.22}_{-1.61}$
Gaia19bjq	A	$0.39^{+0.08}_{-0.07}$	$0.38^{+0.07}_{-0.06}$	$0.34^{+0.31}_{-0.15}$	$0.34^{+0.28}_{-0.14}$	$2.46^{+0.40}_{-0.34}$	$2.71^{+0.39}_{-0.32}$	$2.05^{+0.89}_{-0.69}$	$2.27^{+1.07}_{-0.85}$
Gaia19brt	A	$0.81^{+0.15}_{-0.09}$	$0.99^{+0.14}_{-0.11}$	$0.78^{+0.50}_{-0.30}$	$0.60^{+0.32}_{-0.26}$	$4.42^{+0.40}_{-0.43}$	$5.96^{+0.96}_{-0.74}$	$4.11^{+0.63}_{-0.79}$	$5.89^{+2.11}_{-1.58}$
Gaia19chi	A	$0.63^{+0.08}_{-0.06}$	$0.75^{+0.11}_{-0.08}$	$0.56^{+0.33}_{-0.27}$	$0.50^{+0.28}_{-0.21}$	$1.57^{+0.20}_{-0.13}$	$4.37^{+0.90}_{-0.49}$	$1.60^{+0.31}_{-0.28}$	$3.07^{+1.23}_{-0.88}$
	B	$0.54^{+0.09}_{-0.06}$	$0.62^{+0.08}_{-0.08}$	$0.35^{+0.33}_{-0.17}$	$0.34^{+0.28}_{-0.16}$	$1.18^{+0.25}_{-0.16}$	$2.61^{+0.95}_{-0.57}$	$1.36^{+0.35}_{-0.33}$	$2.32^{+1.05}_{-0.80}$
Gaia19cyv	A	$0.08^{+0.00}_{-0.01}$	$0.08^{+0.01}_{-0.01}$	$0.09^{+0.15}_{-0.03}$	$0.08^{+0.09}_{-0.05}$	$2.21^{+0.23}_{-0.12}$	$2.60^{+0.17}_{-0.18}$	$1.62^{+0.46}_{-0.70}$	$1.88^{+0.76}_{-0.76}$
	B	$0.08^{+0.00}_{-0.01}$	$0.08^{+0.01}_{-0.00}$	$0.14^{+0.18}_{-0.07}$	$0.11^{+0.09}_{-0.05}$	$2.53^{+0.19}_{-0.16}$	$3.68^{+0.19}_{-0.25}$	$1.70^{+0.67}_{-0.57}$	$2.01^{+0.72}_{-0.72}$
Gaia19dae	A	$0.67^{+0.12}_{-0.08}$	$0.71^{+0.10}_{-0.08}$	$0.61^{+0.30}_{-0.26}$	$0.45^{+0.31}_{-0.20}$	$1.63^{+0.22}_{-0.17}$	$2.49^{+0.42}_{-0.28}$	$1.66^{+0.35}_{-0.31}$	$2.54^{+1.18}_{-0.98}$
	B	$0.88^{+0.15}_{-0.13}$	$0.79^{+0.08}_{-0.10}$	$0.83^{+0.45}_{-0.32}$	$0.67^{+0.29}_{-0.26}$	$3.23^{+0.30}_{-0.28}$	$3.08^{+0.17}_{-0.28}$	$1.84^{+0.30}_{-0.28}$	$3.25^{+1.30}_{-1.24}$
Gaia19dak	A	$0.09^{+0.01}_{-0.01}$	$0.09^{+0.01}_{-0.01}$	$0.27^{+0.07}_{-0.17}$	$0.27^{+0.06}_{-0.14}$	$2.72^{+0.20}_{-0.15}$	$4.03^{+0.32}_{-0.28}$	$1.47^{+0.99}_{-0.26}$	$1.40^{+0.49}_{-0.33}$
	B	$0.18^{+0.02}_{-0.03}$	$0.25^{+0.05}_{-0.06}$	$0.28^{+0.09}_{-0.07}$	$0.31^{+0.15}_{-0.08}$	$2.43^{+0.27}_{-0.21}$	$2.37^{+0.53}_{-0.34}$	$1.72^{+0.66}_{-0.28}$	$1.58^{+0.63}_{-0.45}$
Gaia19drc	A	$0.39^{+0.05}_{-0.04}$	$0.41^{+0.04}_{-0.04}$	$0.37^{+0.02}_{-0.02}$	$0.37^{+0.02}_{-0.03}$	$1.28^{+0.10}_{-0.11}$	$1.47^{+0.13}_{-0.13}$	$1.43^{+0.11}_{-0.09}$	$1.04^{+0.28}_{-0.06}$
Gaia19dtd	A	$0.19^{+0.12}_{-0.07}$	$0.21^{+0.09}_{-0.06}$	$0.55^{+0.31}_{-0.19}$	$0.51^{+0.31}_{-0.26}$	$6.21^{+1.03}_{-0.74}$	$9.14^{+1.01}_{-1.62}$	$4.90^{+1.30}_{-1.32}$	$5.06^{+1.30}_{-1.66}$
	B	$0.15^{+0.06}_{-0.04}$	$0.17^{+0.07}_{-0.06}$	$0.74^{+0.31}_{-0.22}$	$0.80^{+0.30}_{-0.29}$	$9.68^{+0.46}_{-0.54}$	$11.21^{+0.70}_{-0.96}$	$5.57^{+0.83}_{-0.72}$	$5.59^{+1.50}_{-1.20}$
Gaia19dtk	A	$0.36^{+0.10}_{-0.07}$	$0.40^{+0.14}_{-0.09}$	$0.31^{+0.29}_{-0.15}$	$0.31^{+0.29}_{-0.16}$	$1.27^{+0.46}_{-0.36}$	$1.52^{+0.64}_{-0.45}$	$1.88^{+1.19}_{-0.74}$	$1.86^{+1.64}_{-0.74}$
	B	$0.49^{+0.10}_{-0.09}$	$0.60^{+0.14}_{-0.11}$	$0.27^{+0.29}_{-0.14}$	$0.26^{+0.27}_{-0.14}$	$1.75^{+0.66}_{-0.48}$	$2.62^{+2.07}_{-0.60}$	$1.90^{+1.07}_{-0.67}$	$1.90^{+1.32}_{-0.68}$
Gaia19dur	A	$0.10^{+0.02}_{-0.01}$	$0.10^{+0.02}_{-0.01}$	$0.39^{+0.31}_{-0.18}$	$0.44^{+0.31}_{-0.19}$	$4.59^{+0.40}_{-0.41}$	$6.56^{+0.74}_{-0.93}$	$2.79^{+1.07}_{-0.76}$	$2.75^{+1.36}_{-0.97}$
Gaia19duw	A	$0.55^{+0.06}_{-0.07}$	$0.51^{+0.09}_{-0.09}$	$0.28^{+0.21}_{-0.12}$	$0.29^{+0.23}_{-0.13}$	$1.29^{+0.41}_{-0.29}$	$2.05^{+0.93}_{-0.56}$	$2.04^{+1.00}_{-0.65}$	$1.82^{+1.03}_{-0.64}$
Gaia19eca	A	$0.13^{+0.04}_{-0.02}$	$0.18^{+0.03}_{-0.02}$	$0.10^{+0.03}_{-0.03}$	$0.05^{+0.03}_{-0.02}$	$4.21^{+0.33}_{-0.59}$	$4.03^{+0.36}_{-0.34}$	$3.75^{+0.39}_{-0.34}$	$5.92^{+0.98}_{-0.80}$
Gaia19ect	A	$0.09^{+0.01}_{-0.01}$	$0.09^{+0.01}_{-0.01}$	$0.04^{+0.39}_{-0.01}$	$0.10^{+0.04}_{-0.04}$	$5.14^{+0.29}_{-0.34}$	$5.51^{+0.39}_{-0.41}$	$6.63^{+0.84}_{-1.74}$	$3.39^{+3.55}_{-1.11}$
Gaia19eim	A	$0.36^{+0.09}_{-0.08}$	$0.51^{+0.12}_{-0.11}$	$0.54^{+0.41}_{-0.23}$	$0.72^{+0.29}_{-0.26}$	$1.61^{+0.52}_{-0.41}$	$4.24^{+1.91}_{-1.51}$	$1.48^{+0.34}_{-0.36}$	$3.63^{+1.82}_{-1.49}$
Gaia19eku	A	$0.59^{+0.12}_{-0.09}$	$0.62^{+0.11}_{-0.09}$	$0.42^{+0.42}_{-0.24}$	$0.43^{+0.43}_{-0.24}$	$4.79^{+1.56}_{-1.13}$	$5.68^{+2.91}_{-1.57}$	$4.63^{+1.66}_{-1.34}$	$4.72^{+2.25}_{-1.57}$
Gaia19enj	A	$0.24^{+0.08}_{-0.08}$	$0.27^{+0.09}_{-0.08}$	$0.25^{+0.25}_{-0.13}$	$0.25^{+0.27}_{-0.12}$	$2.56^{+0.77}_{-0.72}$	$3.38^{+1.50}_{-1.12}$	$2.71^{+0.99}_{-0.92}$	$2.41^{+1.47}_{-0.90}$
Gaia19esp	A	$0.76^{+0.10}_{-0.08}$	$0.75^{+0.17}_{-0.10}$	$0.71^{+0.20}_{-0.15}$	$0.67^{+0.23}_{-0.16}$	$3.40^{+0.59}_{-0.50}$	$4.44^{+0.85}_{-0.66}$	$2.92^{+0.79}_{-0.51}$	$2.34^{+0.69}_{-0.58}$
Gaia19evd	A	$0.66^{+0.11}_{-0.11}$	$0.75^{+0.15}_{-0.10}$	$0.37^{+0.40}_{-0.21}$	$0.45^{+0.42}_{-0.25}$	$3.30^{+0.69}_{-0.76}$	$5.45^{+1.67}_{-1.33}$	$2.68^{+0.66}_{-0.73}$	$5.05^{+3.25}_{-2.00}$
Gaia19fnb	A	$0.58^{+0.14}_{-0.09}$	$0.72^{+0.13}_{-0.11}$	$0.28^{+0.32}_{-0.15}$	$0.29^{+0.32}_{-0.16}$	$2.44^{+0.97}_{-0.73}$	$6.25^{+1.42}_{-1.35}$	$2.37^{+0.91}_{-0.77}$	$3.61^{+1.90}_{-1.41}$

Notes. Parameters are reported as $x^{+\sigma_+}_{-\sigma_-}$, with uncertainties corresponding to the 16th and 84th percentiles.

Appendix C: BHTOM observations

Table C.1. Events observed by each instrument used for follow-up of the GSA microlensing events.

Telescope Name/Code	Events Observed
TRT SBO 70-cm	Gaia18dif, Gaia19bcm
TRT TNO 50-cm	Gaia17aqu
PROMPT8 60-cm	Gaia18bmt, Gaia18cjk, Gaia18dep
LCO coj 100-cm	Gaia17aqu, Gaia17bbs, Gaia17bdk, Gaia18bmt, Gaia18dif, Gaia18eaz, Gaia18cjk, Gaia18dep, Gaia19esp
LCO coj 200-cm	Gaia18bmt, Gaia19eim, Gaia19evd, Gaia19fnb
LCO cpt 100-cm	Gaia17aqu, Gaia17bbs, Gaia17bdk, Gaia18bmt, Gaia18dif, Gaia18eaz, Gaia18cjk, Gaia19esp
LCO lsc 100-cm	Gaia17aqu, Gaia17bbs, Gaia17bdk, Gaia18bmt, Gaia18dif, Gaia18eaz, Gaia18cjk, Gaia18dep, Gaia19esp
LCO ogg 200-cm	Gaia19dak, Gaia19evd
SMARTS 130-cm	Gaia17bej, Gaia18ajt, Gaia18bmt, Gaia18clg, Gaia18cov, Gaia18dep, Gaia18dif, Gaia18eaz, Gaia19aqw
Rapid Eye Mount 60-cm	Gaia18bmt, Gaia18cjk, Gaia18dep, Gaia18eaz, Gaia19aqw
TÜBİTAK T 100-cm	Gaia18cjk
Ondrejov 50-cm	Gaia18cjk, Gaia18cmk
Joan Oró Telescope 80-cm	Gaia18cjk, Gaia18cmk
Molėtai 165-cm	Gaia18cmk
C2PU 104-cm	Gaia18cmk
pt5m 50-cm	Gaia18cmk, Gaia19dak
Aristarchos 230-cm	Gaia19cyv, Gaia19dak
Loiano 152-cm	Gaia19cyv, Gaia19dak

Table C.2. Instruments used for ground-based follow-up of the GSA microlensing events.

Telescope Name/Code	Observatory Name	Location	Long. [deg]	Lat. [deg]	Alt. [m]	Reference
TRT SBO 70-cm	Springbrook Observatory	New South Wales, Australia	149.1	-31.3	1020	-
TRT TNO 50-cm	Thai National Observatory	Chiang Mai, Thailand	98.48	18.57	2450	-
PROMPT8 60-cm	Cerro Tololo Inter-American Observatory	Coquimbo, Chile	-70.8	-30.2	2286	Reichart et al. (2005)
LCO coj 100-cm	Siding Spring Observatory	Siding Spring, Australia	149.1	-31.3	1165	Brown et al. (2013)
LCO coj 200-cm	Siding Spring Observatory	Siding Spring, Australia	149.1	-31.3	1165	Brown et al. (2013)
LCO cpt 100-cm	South African Astronomical Observatory	Sutherland, South Africa	20.8	-32.4	1760	Brown et al. (2013)
LCO lsc 100-cm	Cerro Tololo Inter-American Observatory	Coquimbo, Chile	-70.8	-30.2	2201	Brown et al. (2013)
LCO ogg 200-cm	Haleakalā Observatory	Maui, USA	-156.2560	20.7075	3055	Brown et al. (2013)
SMARTS 130-cm	Cerro Tololo Inter-American Observatory	Coquimbo, Chile	-70.8	-30.2	2215	-
Rapid Eye Mount 60-cm	La Silla Observatory	Coquimbo, Chile	-70.7	-29.3	2400	Zerbi et al. (2004)
TÜBİTAK T 100-cm	TÜBİTAK National Observatory	Antalya, Turkey	30.3356	36.8242	2500	-
Ondrejov 50-cm	Ondřejov Observatory	Ondřejov, Czech Republic	14.7814	49.9094	527	Štrobl et al. (2023)
Joan Oró Telescope 80-cm	The Montsec Observatory	Montsec, Spain	0.7297	42.0517	1570	Domènech Rams et al. (2025)
Molėtai 165-cm	Molėtai Astronomical Observatory	Kulionys, Lithuania	25.5631	55.3159	200	-
C2PU 104-cm	Observatoire de la Côte d'Azur	Calern, France	6.9230	43.7537	1260	-
pt5m 50-cm	Roque de los Muchachos Observatory	La Palma, Spain	-17.8792	28.7606	2326	Hardy et al. (2015)
Aristarchos 230-cm	Helmos Observatory	Klitoria, Greece	22.1983	37.9856	2340	Xilouris et al. (2025)
Loiano 152-cm	Loiano Observatory	Bologna, Italy	11.3344	44.2591	785	-